

Self-Organized Criticality in Stellar Flares

MARKUS J. ASCHWANDEN¹ AND MANUEL GÜDEL²

¹*Solar and Stellar Astrophysics Laboratory (LMSAL), Palo Alto, CA 94304, USA*

²*University of Vienna, Astrophysics Department, Türkenschanzstrasse 17, 1180 Vienna, Austria*

ABSTRACT

Power law size distributions are the hallmarks of nonlinear energy dissipation processes governed by self-organized criticality. Here we analyze 75 data sets of stellar flare size distributions, mostly obtained from the *Extreme Ultra-Violet Explorer (EUVE)* and the *Kepler* mission. We aim to answer the following questions for size distributions of stellar flares: (i) What are the values and uncertainties of power law slopes? (ii) Do power law slopes vary with time? (iii) Do power law slopes depend on the stellar spectral type? (iv) Are they compatible with solar flares? (v) Are they consistent with self-organized criticality (SOC) models? We find that the observed size distributions of stellar flare fluences (or energies) exhibit power law slopes of $\alpha_E = 2.09 \pm 0.24$ for optical data sets observed with Kepler. The observed power law slopes do not show much time variability and do not depend on the stellar spectral type (M, K, G, F, A, Giants). In solar flares we find that background subtraction lowers the uncorrected value of $\alpha_E = 2.20 \pm 0.22$ to $\alpha_E = 1.57 \pm 0.19$. Furthermore, most of the stellar flares are temporally not resolved in low-cadence (30 min) Kepler data, which causes an additional bias. Taking these two biases into account, the stellar flare data sets are consistent with the theoretical prediction $N(x) \propto x^{-\alpha_x}$ of self-organized criticality models, i.e., $\alpha_E = 1.5$. Thus, accurate power law fits require automated detection of the inertial range and background subtraction, which can be modeled with the generalized Pareto distribution, finite-system size effects, and extreme event outliers.

Keywords: Stellar flares — Solar flares — Scaling laws

1. INTRODUCTION

Statistical observations of stellar flares started in the years of 1966-1972 with ground-based spectroscopy in optical wavelengths (Moffett 1974; Moffett and Bopp 1976; Lacy et al. 1976), and was then extended to *extreme ultra-violet (XUV)* wavelengths with space-based instruments such as EXOSAT, the *Extreme Ultra-Violet Explorer (EUVE)*, Chandra, ROSAT, ASCA, the Hubble Space Telescope (HST), and the Newton *X-ray Multi-Mirror Mission (XMM-Newton)* (Collura et al. 1988; Pallavicini et al. 1990; Osten and Brown 1999; Robinson et al. 1999; Audard et al. 1999, 2000; Kashyap et al. 2002). A handicap of space-based observations is the sparse time coverage of stellar flares, which severely restricts the measurement of power law slopes of flare energy distributions to small scale-free (i.e., inertial) energy ranges. Consequently, sophisticated modeling attempts have been developed to extract power law slopes from small flare samples with $\approx 5 - 15$ events only (Audard et al. 1999, 2000; Kashyap et al. 2002; Güdel et al. 2003; Arzner and Güdel 2004; Arzner et al. 2007; Stelzer et al. 2007). One motivation of power law modeling of stellar flare size distributions is the fact that a power law slope of $\alpha \approx 2$ represents a critical value that decides whether the total energy of a size distribution diverges at the largest flares (if $\alpha < 2$), or whether it diverges at the smallest flares (so-called nanoflares) (if $\alpha > 2$). The critical divergence to infinity, however, goes away if one restricts the energy integral to observed energy ranges only, rather than extrapolating to un-observed size ranges. The extrapolation of the power law to unobserved energies that are many orders of magnitude smaller remains questionable (Benz and Krucker 2002). Nevertheless, extrapolation of nanoflare size distributions from small to large flares provides almost sufficient energy

flux to heat the corona (Audard et al. 1999, 2000; Kashyap et al. 2002; Güdel et al. 2003; Arzner and Güdel 2004; Stelzer et al. 2007).

This all changed with the advent of the Kepler mission (Borucki et al. 2010), providing a stellar flare catalog with 162,262 events today, which due to the large statistics allows now very accurate determinations of the power law slope of flare size distributions (Maehara et al. 2012; Shibayama et al. 2013; Aschwanden 2015; Wu et al. 2015; Davenport 2016; **Van Doorselaere et al. 2017**; Yang and Liu 2019). Indeed, fitting a power law distribution to the entire Kepler data set yields a very small statistical error, i.e., $\alpha = 1.817 \pm 0.005$, which appears to be much smaller than systematic errors due to truncation effects, instrumental sensitivity limitations, incomplete sampling, background subtraction effects, arbitrary inertial ranges, and finite-system size effects (Aschwanden 2015). Theoretically and observationally, there is evidence for two types of white-light emission during flares (non-thermal beam heating versus thermal continuum emission), which implies a prompt as well as a delayed component, with possibly different power law slopes of their size distributions.

On the modeling side we have to ask whether the value of the power law slope depends on the stellar spectral type, the age and size of the star, the rotation rate, and the time variability (quiescent versus flaring time intervals). In this study we investigate some of these effects, in order to improve the observed value of the power law slope and to test theoretical *Self-organized criticality* (SOC) models. One modification of the standard SOC model is the Dragon-King hypothesis (Sornette 2009; Sornette and Ouillon 2012), which suggests that the most extreme events in a statistical distribution may belong to a different population, and thus may be generated by a different physical mechanism, in contrast to the strict power law behavior of standard SOC models. Occasional evidence was found for such a Dragon-King concept in solar and in stellar flare data sets with large statistics (Aschwanden 2019, 2021).

The content of this paper includes a compilation of observations of stellar flares (Section 2, Tables 1-2), examples of size distribution modeling (Section 3), statistical results (Section 4), discussion of relevant literature (Section 5), and conclusions (Section 6).

2. OBSERVATIONS OF STELLAR FLARES

We compile 20 studies that contain statistics of stellar flare radiated energies E , in form of occurrence frequency distributions $N(E) \propto E^{-\alpha}$, with fitted power law slopes α (see Tables 1 and 2). Stellar flares are generally defined in terms of temporary increases of the observed flux above the pre-flare and post-flare quiescent level. The flare energy E is often estimated from the fluence or total counts (in a given wavelength), which is defined as the time integral of the flux (intensity or luminosity) over the flare duration. Some data sets contain flares from a single star only, while other data sets combine flare events from different stars of the same stellar spectral type. In cases where the cumulative size distribution is given (with slope β), we convert it to the slope $\alpha = (\beta + 1)$ of the differential size distribution. For the uncertainty σ_α of the power law slope we use the generic relationship $\sigma_\alpha = \alpha/\sqrt{n_{ev}}$ (Clauset 2009), where n_{ev} represents the number of flare events that contribute to the linear regression fit of the power law slope. In Tables 1 and 2 and in this Section we summarize the instruments, the spectral types of the stellar classification, the number of flare events per data set, the physical parameter used in the energy definition (count rate, total counts, time-integrated radiated energy, or peak flux rate), and the power law slopes of energies with uncertainties.

Observations of 409 stellar flares have been obtained during 469 hours from 8 UV Ceti-type (cool dwarf) flare stars (CN Leo, UV Cet, Wolf 424 AB, YZ CMi, EQ Peg, EV Lac, AD Leo, YY Gem) in optical wavelengths (U, B, V band, $\lambda = 3370 - 5550 \text{ \AA}$), observed at the McDonald Observatory (Moffett 1974; Lacy et al. 1976). The flare energies E were calculated from the observed (time-integrated) fluences (or luminosities) for each star separately, yielding cumulative power law distributions with slopes in the range of $\beta = 0.43 - 1.00$, which we convert to differential size distributions with $\alpha = \beta + 1 = 1.43 - 2.00$ (**Moffett 1974; Lacy et al. 1976**). A similar data set of 21 flares occurring on 13 different dMe stars was observed in soft X-rays with EXOSAT (in soft X-ray energies of 0.05 - 2 keV), yielding a power law distribution of the soft X-ray peak flux $\alpha_P = 1.52$ (Collura et al. 1988), and $\alpha_P = 1.7$ (Pallavicini et al. 1990). These two studies are the only ones that used a peak flux (in units of energy per time), rather than a total (time-integrated) energy as quoted in all other observations in this study. An analysis of 16 RS CVn binary star systems (G, F, K-types) was undertaken with *Extreme Ultraviolet Explorer* (EUVE) photometry, yielding a power law slope of energies $\alpha_E = 1.60$, where the flare energy is proportional to the time-integrated counts (Osten and Brown 1999). Photometric observations of the dM4.5e flare star YZ CMi using the *Hubble Space Telescope* in the ultraviolet wavelength range of ($\lambda = 1600 - 3200 \text{ \AA}$) detected 54 flare events and yielded an energy distribution with a power law-like slope of $\alpha = 2.25$ (Robinson 1999). Further observations with EUVE targeted two active solar analogs, 47

Cas and EK Dra, gathering 28 flares and a power law slope of $\alpha \approx 2.2 \pm 0.2$ for the flare energies estimated from the total counts (Audard et al. 1999). Twelve data sets of cool dwarf stars i.e., HD 2726, 47 Cas, EK Dra, κ Cet (1994, 1995), AB Dor, ϵ Eri, GJ 411, AD Leo, CN Leo (1994, 1995), were observed with EUVE, leading to power law slopes in the range of $\alpha \approx 1.53 - 2.39$ (Audard et al. 2000). One study focused on relatively weak flares from cool dwarfs FK Aqr (dM2e type), V1054 Oph (M3Ve type), and AD Leo (M3 V type), and found power law slopes of $\alpha \approx 2.60, 2.74,$ and $2.03-2.32$, using EUVE deep survey data (Kashyap et al. 2002). Observations with EUVE concentrate on the cool dwarf AD Leo in several studies (Kashyap et al. 2002; Güdel et al. 2003; Arzner and Güdel 2004), applying different statistical models, which converge to similar values for the power law slope in the range of $\alpha \approx 2.25-2.30$. Two other studies detected soft X-ray emission from stellar flares using the XMM-Newton telescope, performing observations in the Taurus molecular cloud (Arzner et al. 2007; Stelzer et al. 2007).

On March 7, 2009, the Kepler space telescope was launched (Borucki et al. 2010), which was designed to survey the stars and planets in the Milky Way galaxy, in particular the exoplanets that orbit around other stars than our Sun. It turned out that the study of the light curves reveals numerous stellar flare events, superimposed on the relatively slow rotational modulation. At the time of writing, the Kepler flare catalog contains 3420 flare stars and 162,262 flare events (Yang and Liu 2019). **The number of detected flares strongly depends on the detection algorithm. For instance, the study of Van Doorselaere et al. (2017) detected 16,850 flares on 6662 stars out of a total of 188,837 in the Kepler field-of-view during Q15.** We provide a compilation of Kepler flare statistics in Table 2, based on the studies of Maehara et al. 2012; Shibayama et al. 2013; Balona 2015; Aschwanden 2015, 2019, 2021; Wu et al. 2015, Davenport 2016, and Yang and Liu 2019). These new measurements from Kepler represent an enormous breakthrough in the statistical accuracy of stellar flares, which enables us to determine the power law distributions of stellar flare energies in different stellar types. However, one particular property is the wavelength range of Kepler observations, which is in the optical wavelength regime ($\lambda = 4300 - 8900 \text{ \AA}$), roughly corresponding to white-light flares observed on the Sun. We have to keep this optical wavelength bias in mind when we compare with observations in soft X-rays and EUV (EXOSAT, EUVE, XMM-Newton). Also, there may be a possible wavelength dependence in the related power law slopes. The flare events have been detected with Kepler using different methods that are described in Davenport (2016) and Yang and Liu (2019) and are subject to various biases and false-positive signals. Examples of such erroneous signals are periodic flux modulations from RR Lyrae, pulsating giants, eclipsing binaries, or fluctuations from δ Scuti and γ Doradus stars. Size distributions of flare-radiated energies are gathered for flares from the same star (given by the KID identification number in Table 2), as well as for different stellar spectral types (A, F, G, K, M-type, Giants) separately.

3. SIZE DISTRIBUTION MODELING

The primary goal of our analysis is a deeper physical understanding of size (or occurrence frequency) distributions of stellar flares, which we can study now thanks to the revolutionary *Kepler* mission data (Yang and Liu 2019), with larger statistics and superior data quality than previously achieved with solar flare data. Solar data make up for a small subset of stellar data only. We expect that size distributions of solar and solar-like stars should be similar (besides their amplitude that varies with the magnetic cycle), while it is an open question whether other stellar types have different size distributions than solar-like stars. In the following we describe state-of-the-art power law fitting methods of size distributions, applied here to data from the Kepler stellar flare catalog. For more methodical details see also Aschwanden (2011, Section 7).

3.1. Differential Size Distribution

A *size distribution* of events, $N(x)dx$, also called a *differential occurrence frequency distribution*, can ideally be approximated by a power law as a function of some size parameter x , quantified by four parameters $(x_1, x_2, n_0, \alpha_x)$,

$$N(x)dx = n_0 x^{-\alpha_x} dx, \quad x_1 \leq x \leq x_2, \quad (1)$$

where x_1 and x_2 are the lower and upper bounds of the power law inertial (or scale-free) range, α_x is the power law slope, and n_0 is a normalization constant. Uncertainties in the calculation of the power law slope mostly result from the arbitrary choice of the fitting range $[x_1, x_2]$, which can be largely eliminated by a generalized power law function that includes under-sampling at the lower end and finite system size effects at the upper end of the inertial range $[x_1, x_2]$.

3.2. Thresholded Power Law Distribution

The ideal power law function (Eq. 1) can be generalized with an additional “shift” parameter x_0 (with respect to x), also called *Lomax distribution* (Lomax 1954), *Generalized Pareto distribution* (Hosking and Wallis 1987), or *Thresholded power law size distribution* (Aschwanden 2015),

$$N(x)dx = n_0 (x_0 + x)^{-\alpha_x} dx, \quad x_1 \leq x \leq x_2, \quad (2)$$

with the normalization constant n_0 . This additional parameter x_0 accomodates three different features: truncation effects due to incomplete sampling of events below some threshold (if $x_0 > 0$), incomplete sampling due to instrumental sensitivity limits (if $x_0 > 0$), or subtraction of event-unrelated background (if $x_0 < 0$), as it is common in astrophysical data sets (for details see Aschwanden 2015). The differential size distribution (Eq. 2) fitted to the flare energies of the Kepler events is shown in Fig. (1b) for the Pareto model, in Fig. 2b for the finite-system model, and in Fig. 3b for the extreme event model.

3.3. Cumulative Size Distribution

While Eqs. (1) and (2) represent a *differential size distribution* $N_{diff}(x)$, it is statistically more advantageous to employ *cumulative size distributions* $N_{cum}(> x)$, especially for small data sets and near the upper cutoff, where we deal with a small number of events per bin. We will use cumulative size distributions that include all events accumulated above some size x , such as for the *thresholded power law size distribution*,

$$N_{cum}(> x) = \int_x^{x_2} n_0(x + x_0)^{-\alpha_x} dx = 1 + (n_{ev} - 1) \left(\frac{(x_2 + x_0)^{1-\alpha_x} - (x + x_0)^{1-\alpha_x}}{(x_2 + x_0)^{1-\alpha_x} - (x_1 + x_0)^{1-\alpha_x}} \right), \quad (3)$$

with n_{ev} the number of events. We show an example of a size distribution that contains the counts of events per bin $n_{cts}(x)$ in Fig. (1a), the corresponding differential size distribution $N_{diff}(x) = n_{cts}(x)/\Delta x$ in Fig. (1b), and the corresponding cumulative size distribution $N_{cum}(> x)$ in Fig. (1c). The event count histogram (Fig. 1a) defines the inertial range $[x_0, x_2]$, the minimum (x_1), and maximum value (x_2) of the size parameter x , with a peak in the event count histogram at x_0 (Fig. 1a), which provides a suitable threshold definition, because incomplete sampling of small values $x < x_0$ is manifested by the drop of detected events on the left side of the peak x_0 . This definition of a threshold x_0 has been proven to be very useful for characterizing data sets with incomplete or sensitivity-limited sampling (Aschwanden 2015). This provides also a definition for the inertial range $[x_0, x_2]$ in the fitting procedure.

3.4. Rank-Order Plot

An equivalent method to calculate the cumulative size distribution is the *rank-order plot*. If the statistical sample is rather small, in the sense that no reasonable binning of a histogram can be done, either because we do not have multiple events per bin or because the number of bins is too small to represent a distribution function, we can create a rank-order plot. A rank-order plot is essentially an optimum adjustment to small statistics, by associating a single bin to every event. From an event list of a parameter $x_i, i = 1, \dots, n_x$, (e.g., the energies of n_x flares), which is generally not sorted, we have first to generate a rank-ordered **or sorted 1-D array** by ordering the events according to increasing size,

$$x_1 \leq x_2 \leq \dots \leq x_j \leq \dots \leq x_n, \quad j = 1, \dots, n. \quad (4)$$

The bins are generally not equidistant, neither on a linear nor a logarithmic scale, defined by the difference between subsequent values of the ordered series x_j ,

$$\Delta x_j^{bin} = x_{j+1}^{bin} - x_j^{bin}. \quad (5)$$

In a rank-ordered sequence of n_x events, the probability for the largest value is $1/n_x$, for events that are larger than the second-largest event it is $2/n_x$, and so forth, while events larger than the smallest event occur in this event list with a probability of unity. Thus, the cumulative frequency distribution is simply the reversed rank order,

$$N_{cum}(> x_j) = (n_x + 1 - j), \quad j = 1, \dots, n_x, \quad (6)$$

and the distribution varies from $N_{cum}(> x_1) = n_x$ for $j = 1$, to $N_{cum}(> x_n) = 1$ for $j = n_x$.

We can thus plot a cumulative frequency distribution with $N_{cum}(> x_j)$ on the y-axis versus the size x_j on the x-axis. The cumulative distribution functions $N_{cum}(> x)$ (Eq. 6) of our 3 models for the example of Kepler flares is displayed

in form of histograms in Figs. 1c, 2c, and 3c, while the 5 highest rank-ordered bins $N_{cum}(> x_j)$ are marked with diamonds in Figs. 1c, 2c, and 3c.

The distribution is normalized to the number of events n_x ,

$$\int_{x_1}^{x_n} N(x)dx = N_{cum}(> x_1) = n_x . \quad (7)$$

We overlay rank-order bins in the cumulative size distribution of Fig. (1c) (shown with black diamond symbols), for the 5 most extreme events of this size distribution. While the best fit of the *generalized Pareto distribution* yields a good fit in the inertial range between $x_0 = 6.41 \times 10^{33}$ and $x \approx 10^{37}$ erg, we notice a significant deviation in the range above $x \gtrsim 10^{37}$ erg, which we will model in the following. The self-consistency between the differential and the cumulative size distribution is very high, with almost identical power law slopes of $\alpha_{diff} = 1.863 \pm 0.005$ (Fig. 1b) and $\alpha_{cum} = \beta_{cum} + 1 = 1.877 \pm 0.005$ (Fig. 1c), differing by $\lesssim 0.7\%$ only. **This statistical uncertainty (or formal error) appears to be much smaller than systematic errors due to truncation effects, instrumental sensitivity limitations, incomplete sampling, background subtraction effects, arbitrary inertial ranges, and finite-system size effects (Aschwanden 2015).**

3.5. Finite-System Size Effects

The size distribution can be uniquely approximated with a classical power law function, if the lower bound (x_1) and upper bound (x_2) are well-defined. In practice, however, the lower bound is flattened by undersampling, detection thresholds, or instrumental sensitivity limitations, while the upper bound typically shows a gradual steepening due to finite-system effects (Pruessner 2012). Ignoring these effects leads to power law fits with arbitrary inertial ranges $[x_0, x_2]$, which affects the accuracy of the determined power law slope and its uncertainty. Finite-system effects are generally modeled with an exponential cutoff function (Pruessner 2012), which we can combine with the generalized Pareto distribution (Eq. 2),

$$N(x)dx = n_0 (x_0 + x)^{-\alpha_x} \exp\left(-\frac{x}{x_e}\right) dx , \quad (8)$$

quantified with the exponential function $\exp(-x/x_e)$, where x_e is a free variable when fitting Eq. (8). Thanks to the large statistics of Kepler-observed stellar flares, this zone at the upper bound of the size distribution is not sparsely sampled and can be accurately modeled. We perform the modified power law fit functions in Fig. 2, which clearly show an improvement of our size distribution function (Eq. 8) at the upper end between $E \approx 10^{36}$ erg and $E \approx 2 \times 10^{37}$ erg, which shows a least-square χ^2 fit improving from $\chi_{diff} = 4.5$ (Fig. 1b) to $\chi_{diff} = 1.5$ (Fig. 2b). The inclusion of finite-size effects changes the power law slope from $\alpha_E = 1.863 \pm 0.005$ to $\alpha_E = 1.817 \pm 0.005$ (a decrease of -2.5%) for the differential size distribution, and $\alpha_E = 1.877 \pm 0.005$ to $\alpha_E = 1.823 \pm 0.005$ (a decrease of -2.9%) for the cumulative size distribution (Figs. 1c and 2c). Thus we conclude that inclusion of finite-system size effects can change the power law slope by a few percents.

3.6. Extreme Events

Inspecting the residuals of the power law fits in Fig. 2 we notice an excess of events at energies of $E \approx (1 - 4) \times 10^{38}$ erg that cannot be fitted with the exponential drop-off function, as expected from finite-system size effects in the extreme-event zone. These extreme events that deviate from a standard power law distribution function have also been dubbed as “*Dragon-King*” events by Sornette (2009) and Sornette and Ouillon (2012), who suggested that they are generated by a different physical mechanism. Detections of such extreme event outliers have occasionally been noted in astrophysical data sets (Aschwanden 2019).

We model the size distribution with two power law components, where the first power law distribution includes the exponential function (Eq. 8) with amplitude $(1 - q_{pow})$, while the second power law distribution with amplitude (q_{pow}) extends all the way to the largest event (with an identical power law slope),

$$N(x)dx = n_0 (x_0 + x)^{-\alpha_x} \left[(1 - q_{pow}) \exp\left(-\frac{x}{x_e}\right) + q_{pow} \right] dx , \quad (9)$$

where we define the exponential cutoff energy with $x_e = x_2 q_{exp}$. This combinatory definition of the size distribution converges to the canonical finite-system size distribution as defined in Eq. (8), for $q_{pow} \mapsto 0$. We show the best fit of

this model for extreme events in Fig. 3. The χ^2 -values amount to $\chi_{diff}^2 = 1.50$ (Fig. 3b) and $\chi_{cum}^2 = 0.80$ (Fig. 3c). The resulting free parameters are $\alpha_{diff} = 1.817 \pm 0.005$ (Fig. 3b), $\alpha_{cum} = 1.821 \pm 0.005$ (Fig. 3c), $q_{exp} = 0.05$, and $q_{pow} = 0.08$ (Fig. 3b). Thus, the extreme events comprise a fraction of $q_{pow} = 8\%$ of all events at high energies of $x \gtrsim x_e$.

A synopsis of the three models is shown in Fig. 4, depicting the Pareto distribution (P-Model), the finite-system size effect (F-Model), and the extreme event component (E-Model). All three models agree with each other in the inertial range ($\gtrsim x_0, \lesssim x_3$), but the goodness-of-fit is in the order of unity for the Models (F) and (E) only. Obviously the Pareto P-model alone cannot reproduce the high-end tail, which is reflected in the high values of the best-fit χ^2 values (Fig. 1), while the extreme event model (E) yields the best consistency with the observed data (Fig. 3). Note that the best-fitting model (E) has six free parameters ($n_0, a, x_0, x_2, q_{exp}, q_{pow}$). Such a high degree of precision in the fitting of the observed size distribution (Fig. 3) is only feasible with large statistics, such as with the data set of $n_{ev} \gtrsim 10^5$ stellar flares observed with Kepler.

3.7. Estimates of Uncertainties

In the binned power law fitting methods we can assert an uncertainty for the counts per bin from Poisson statistics,

$$\sigma_{diff,i} = \frac{\sqrt{N_i \Delta x_i}}{\Delta x_i}. \quad (10)$$

For the cumulative size distribution, where the difference of events ($N_i - N_{i+1}$) per bin are counted as independent events only (Aschwanden 2015), the uncertainty is,

$$\sigma_{cum,i} = \sqrt{(N_i - N_{i+1})}. \quad (11)$$

Furthermore, the uncertainty σ_α of the best-fit power law slope is estimated to,

$$\sigma_\alpha = \frac{\alpha}{\sqrt{n_{ev}}}, \quad (12)$$

with n_{ev} the total number of events in the entire size distribution (or in the fitted range), according to Monte-Carlo simulations with least-square fitting (Aschwanden 2015). A slightly different estimate of $\sigma_\alpha = (\alpha - 1)/\sqrt{n}$ is calculated in Clauset et al. (2009).

The fitting of any of the 3 models of the differential occurrence size distribution $N_{diff}^{theo}(x)$ to an observed (binned) size distribution $N_{diff}^{obs}(x)$, or of the cumulative size distribution $N_{cum}^{theo}(x)$ to an observed size distribution $N_{cum}^{obs}(x)$, is performed with a standard least-square χ^2 (i.e., reduced χ^2) method. The method and numerical Monte-Carlo simulations of the error estimates are described in more detail in Aschwanden (2015).

4. STATISTICAL RESULTS

Here we present statistics of the means and standard deviations of the reported power law slopes in stellar size distributions (Section 4.1), their dependency on the stellar spectral type (Section 4.2), their time variability (Section 4.3), comparisons between stellar and solar power law slopes (Section 4.4), and the application of self-organized criticality (SOC) models to stellar flare size distributions (Section 4.5).

4.1. Power Law Slopes of Stellar Flares

We present now a comprehensive compilation of power law slopes observed from size distributions of stellar flares (with a total of 75 data sets), as listed in Tables 1 and 2. Table 1 includes 33 data sets from the pre-Kepler (1976-2007) era, and Table 2 lists 42 data sets from the Kepler mission (2009-present). Pre-Kepler observations of stellar flares have been made with the UVB, EXOSAT, EUVE, HSP/HST, and XMM-Newton instruments. When we mention power law slopes of energies detected in different wavelengths (optical, UV, XUV, soft X-rays, or hard X-rays), we should be aware that their slopes are not assumed to be identical, because they are produced by different physical mechanisms.

We display the results of the 75 data sets in form of scatter plot as a function of the sample size (Fig. 5). **All data sets analyzed here and shown in Figs. 5 and 6 are taken from published literature values.** We divide the 75 data sets into three groups sampled in different wavelength ranges: The data set with UVB spectroscopy (Fig. 5a), the data set with XUV fluences, measured with EXOSAT, EUVE, HSP/HST, XMM-Newton (Fig. 5b), and the data

set OPT with optical luminosities (integrated over the flare duration) from Kepler (Fig. 5c). For these three groups we find the following mean and standard deviations (Fig. 5):

$$\alpha_{\text{UBV}} = 1.80 \pm 0.19 , \quad (13)$$

$$\alpha_{\text{XUV}} = 2.08 \pm 0.37 , \quad (14)$$

$$\alpha_{\text{OPT}} = 1.93 \pm 0.40 , \quad (15)$$

In order to eliminate small-number samples we select also large-size distributions with $n_{ev} > 1000$ events (i.e., OPT data set with Kepler data only) and obtain (Fig. 5c),

$$\alpha_{\text{OPT}}(n_{ev} > 1000) = 2.09 \pm 0.24 , \quad (16)$$

which narrows the distribution of α -values from 20% to 10%, while their means are consistent within the uncertainties.

The diagram of Fig. (5c) illustrates the convergence of the distribution of α -values as a function of the sample size n_{ev} . The small-sample α -values spread over a range of $1.5 \lesssim \alpha \lesssim 3$, while the large-sample α -values (with $n_{ev} > 1000$) converge to a range of $1.9 \lesssim \alpha \lesssim 2.3$. This convergence clearly demonstrates that the uncertainty of the power law slope scales with the sample size, as predicted by the uncertainty estimate of Eq. (12) and shown in Fig. (5c) (solid curves).

What is the most accurate value of the fitted power law slopes α ? A compilation of large-number fits can be found in Table 2. The power law slope of all stellar flare events detected by Kepler ($n=162,262$) is $\alpha = 1.817 \pm 0.005$ (Fig. 3b). Inspecting the uncertainties σ_α in Fig. (5c) we notice that small samples (with $n_{ev} \lesssim 1000$) display uncertainties that are commensurable with their deviation from a mean value of $\alpha \approx 2$, while large samples (with $n_{ev} \gtrsim 1000$) display much smaller uncertainties so that they do not overlap with their common mean value, which indicates that there are systematic errors that are not accounted for (such as arbitrary fitting ranges $[x_0, x_2]$ or inaccurate background subtraction). We do correct for under-sampling of weak stellar fluxes (by using the thresholded power law model), as well as for finite-size effects. The cumulative size distribution fit shown in Fig. (1c) clearly shows an anomalous deviation from an ideal power law distribution for the largest events in the range of $x \approx 10^{37}$ erg to 4×10^{38} erg, which can be fitted with the finite-system size model (F) and the extreme event model (E) (Fig. 4).

4.2. Power Law Slopes and Stellar Spectral Types

In the study of Yang and Liu (2019), the stellar flare catalog of the Kepler mission has been sorted according to the spectral type of the observed stars. This enables us to investigate the power law slopes α of the flare size (or energy) distributions for each stellar spectral type (A, F, G, K, M, and Giants) separately. Each spectral type may have different stellar properties. We show the power law slopes α of the various stellar spectral types as a function of the sample size in Fig. 6. Interestingly, all stellar spectral types have power law slopes near $\alpha \approx 2.0$. The largest data sets (with $n_{ev} > 1000$) have the following power law slopes: $\alpha_G = 2.10 \pm 0.21$ for G-type stars (Fig. 6a), $\alpha_F = 2.36 \pm 0.25$ for F-type stars (Fig. 6b), $\alpha_M = 1.99 \pm 0.35$ for M-type stars (Fig. 6c), $\alpha_K = 2.02 \pm 0.33$ for K-type stars (Fig. 6d), and $\alpha_{Giants} = 1.90 \pm 0.10$ for Giant stars (Fig. 6f). The only exception is $\alpha_A = 1.12 \pm 0.08$ for A-type stars (Fig. 6e), as it was noted before (Yang and Liu 2019). This outlier is re-visited in a recent study and it was found to originate most likely from an ill-defined inertial range, while fits with our P, F, and E models yielded a value of $\alpha_A = 1.65 \pm 0.00$ that is more consistent with the other spectral types (Aschwanden 2021), and invalidates the claim of a different physical mechanism made by Yang and Liu (2019). Thus we ignore this dubious value in further analysis.

From the Kepler data shown in Fig. 5c it appears that the data sets with the largest statistics ($n_{ev} > 1000$) with a power law value of $\alpha_{\text{OPT}} = 2.09 \pm 0.24$ seem to cluster around the mean value of $\alpha \approx 2.0$. Given the fact that the same trend holds for all spectral types (Fig. 6), it is conceivable that all stellar types can be explained in terms of a single general model that predicts an universal value of $\alpha \approx 2$.

4.3. Time Variability of Power Law Slopes

We investigate whether there are evolutionary trends of the slopes $\alpha(t)$ as a function of time t , since some observations are made up to 30 years apart (during 1970-2000). From the pre-Kepler data sets (Table 1) we find four cases with substantial time epochs, all observed in M-dwarf stars (CN Leo, YX CMi, EV Lac, and AD Leo). We plot the time evolution of the power law slope $\alpha(t)$ in Fig. 7, which reveals a highly significant time variation for YZ CMi only, but this star was observed with different instruments (i.e., in optical first, and in EUV later on.) The other cases show temporal variations that are commensurable with their uncertainties $\sigma_\alpha = \alpha/\sqrt{n_{ev}}$ (Eq. 12). Hence we do not find much evidence for a time evolution of the power law slopes.

4.4. Stellar versus Solar Power Laws

For the comparison of stellar versus solar size distributions, we use the most extensive data set that is available, obtained from automated flare detection in *soft X-ray (SXR)* wavelengths, using *Geostationary Orbiting Earth Satellite (GOES)* data from over 37 years, amounting to a total of over $n_{ev} \gtrsim 300,000$ flare events (Aschwanden and Freeland 2012). The power law slope α_F of the size distribution of GOES 1-4 Å fluxes has been measured through three (magnetic) solar activity cycles (containing 338,661 automatically detected flare events),

$$\alpha_{F,GOES} = 1.98 \pm 0.11 \quad (17)$$

The soft X-ray fluxes F_{GOES} observed with GOES originate from chromospheric evaporation of heated plasma during a flare process. According to the Neupert effect (Dennis and Zarro 1993), the soft X-ray flux is essentially the time integral of the hard X-ray flux $f_{HXR}(t)$, which represents the heating rate of the soft X-ray emitting plasma,

$$P_{SXR} = \int f_{HXR}(t) dt \approx F_{HXR} T \approx E_{HXR} . \quad (18)$$

This relationship implies identical power law slopes of $\alpha_{P,SXR} = \alpha_{E,HXR}$, which can be used to constrain the free parameters (S, β, γ, D_S) of the FD-SOC model.

The power law slopes obtained from GOES soft X-ray fluxes $\alpha_{F,GOES} = 1.98 \pm 0.11$ (Eq. 17) are similar to those of the UVB data set (Fig. 5a; $\alpha_{UVB} = 1.80 \pm 0.19$), with those in XUV wavelengths (Fig. 5b; $\alpha_{XUV} = 2.08 \pm 0.37$, and with those of the Kepler data sets, with $\alpha_{OPT} = 1.93 \pm 0.40$ for all 40 optical datasets (Fig. 5c), which converges to $\alpha_{OPT} = 2.09 \pm 0.24$ (Fig. 5c) for large data sets with $n_{ev} > 1000$. The self-consistency of power law slopes $\alpha_F \approx 2.0$ corroborates the proportionality ($\gamma \approx 1$) between (optically-thin) fluxes and (fractal) flare volumes (Eq. 24), as assumed in our fractal-diffusive SOC model.

How typical is our Sun among other stars of the same spectral type G? In Fig. (6a) we depict the power law slopes of 13 datasets that comprise stellar flare statistics of solar-like stars, groups that are referred to as G-types (Yang and Liu 2019; Wu et al. 2015), G5-stars (Maehara et al. 2012; Shibayama et al. 2013; Aschwanden 2015), slowly rotating G5-stars (Maehara et al. 2012; Shibayama et al. 2013), and G dwarfs (Audard et al. 1999). The diagram in Fig. (6a) reveals that all of these solar-like data sets of G type are consistent with a power law slope value of $\alpha_F \approx 2$, within the stated uncertainties (as listed in Table 2). The largest of these G-type data sets from Kepler (with $n=55,259$ flare events) displays a value of $\alpha_G = 1.96 \pm 0.04$ (Yang and Liu 2019), which appears to converge to an asymptotic value of the power law slope $\alpha_F \approx 2.0$ (Fig. 6a). Thus, we can conclude that both solar and stellar flares have approximately similar power law slopes in their size distributions, but we have to be aware that solar flares are observed in hard X-rays and soft X-rays, while stellar flares are observed in optical wavelengths here.

4.5. Self-Organized Criticality and Stellar Flares

The concept of *Self-Organized Criticality (SOC)* has been introduced by Bak et al. (1987, 1988) and has been applied to a large number of nonlinear processes in the universe (see textbooks by Aschwanden 2011; Pruessner 2012). In a nutshell, we can characterize SOC models in terms of a critical state of a nonlinear energy dissipation system that is slowly and continuously driven towards a critical value of a system-wide instability threshold, producing scale-free, fractal-diffusive, and intermittent avalanches with powerlaw-like size distributions (as defined in Aschwanden 2014; 2015). Avalanches in such nonlinear systems exhibit an exponential growth phase and a random-like duration, resulting in power law-like size distributions (called scale-free), while the spatio-temporal behavior can exhibit fractal geometry, diffusive transport, and intermittent time structures. Classical paradigms for SOC models are sand avalanches, earthquakes, forest fires, as well as a number of astrophysical processes, such as solar and stellar flares. Our prime question here is whether a SOC model can predict the exact value of the power law slope for stellar flare phenomena, or whether observations of stellar flares can confirm and constrain the power law slopes predicted by SOC models. A secondary question in this study is whether flares on active stars have identical size distributions as solar flares, and thus are likely to be produced by the same physical mechanism.

We follow the concept of a generalized SOC system as defined in Aschwanden (2014). The assumptions made therein consist of the following 6 physical relationships:

(1) The scale-free probability conjecture, which simply says that the number of avalanches $N(L)$ with size L is reciprocal to the length scale L (normalized by L_0), with Euclidean dimension D ,

$$N(L) dL \propto \left(\frac{L}{L_0} \right)^{-D} dL , \quad (19)$$

(2) the Euclidean flare volume V is fractal and has a fractal (Hausdorff) dimension D_d ,

$$V \propto L^{D_d} , \quad (20)$$

(3) the mean fractal dimension D_d is given by the geometric mean of the smallest ($D_{min} \approx 1$) and largest possible fractal dimension $D_{max} \approx D$,

$$D_d \approx \frac{D_{d,min} + D_{d,max}}{2} = \frac{(1 + D)}{2} , \quad (21)$$

(4) the evolution of an avalanche as a function of time duration T grows according to classical diffusion,

$$L \propto T^{\beta/2} \mapsto T \propto L^{2/\beta} , \quad (22)$$

(5) the observed flux F scales with the avalanche volume V with a power law exponent γ ,

$$F \propto V^\gamma , \quad (23)$$

(6) the peak flux is given by avalanche propagation with maximal fractal dimension (D_{max}), and the avalanche energy E is given approximately by the product of the mean flux F and the avalanche duration T ,

$$E = F T . \quad (24)$$

From these 6 assumptions we can derive straightforwardly the predicted power law slopes of the size distributions of a SOC system. Since all relationships given in Eq. (19-24) are expressed in terms of the variable L , the power law indices α_x for the size distribution of the parameters $x = A, V, T, F, P, E$ can be derived by substitution of variables, i.e., $N(x)dx = N[x(L)] |dx/dL| dL \propto x^{-\alpha_x}$, yielding the power law indexes α_x (Aschwanden 2019),

$$\alpha_L = S \approx 3 \quad (25)$$

$$\alpha_A = 1 + (S - 1)/D_2 \approx 7/3 \quad (26)$$

$$\alpha_V = 1 + (S - 1)/D_3 \approx 2 \quad (27)$$

$$\alpha_T = 1 + (S - 1)\beta/2 \approx 2 \quad (28)$$

$$\alpha_F = 1 + (S - 1)/(\gamma D_S) \approx 2 \quad (29)$$

$$\alpha_P = 1 + (S - 1)/(\gamma S) \approx 5/3 \quad (30)$$

$$\alpha_E = 1 + (S - 1)/(\gamma D_S + 2/\beta) \approx 3/2 , \quad (31)$$

where we included the dimensionality of the Euclidean geometry (S), the flare area (A), and the peak flux (P) also. The approximative numerical values are obtained by inserting the default parameters $S = 3, \beta = 1, \gamma = 1, D_2 = 1.5, D_3 = 2$, based on observations (see Aschwanden 2014). In other words, our basic assumptions for SOC avalanches boil down to the three hypotheses of a 3-D Euclidean space ($S = 3$), classical diffusion ($\beta = 1$), and fractal geometry ($D_{min} = 1, D_{max} = 3$).

4.6. Low-Cadence Kepler Data

Since Kepler supposedly measures the (time-integrated) fluences $E \propto F_{\text{SXR}}$ (Eq. 18), we expect a power law slope of $\alpha_E = 1.5$ for the fluence (Eq. 31), rather than the observed value of $\alpha_{\text{F,GOES}} \approx 2.0$ (Eq. 17). This apparent discrepancy can be reconciled in the case of flare detection with insufficient cadence, i.e., $\Delta T \geq T$, in which case the fluence relationship $E = F T$ (Eq. 24) degenerates to proportionality,

$$E_K \approx F \Delta T \propto F , \quad (32)$$

where the subscript ‘‘K’’ refers to the Kepler-specific low-cadence mode. From the proportionality between the energy E_K and the mean flux F we expect then an identical power law slope,

$$\alpha_{EK} = \alpha_F = 2.0 , \quad (33)$$

since the time cadence ΔT is a constant. Indeed, long-cadence data from Kepler are processed in time intervals ($2\Delta T = 1$ hour) that are substantially longer than the typical duration of solar flares (e.g., $T = 25 \pm 30$ min; Aschwanden

2020). Flare durations on young brown stars observed in the Kepler low-cadence (1 min) mode were found over a range of $T = 0.17 - 8.6$ min (Gizis et al. 2017). However, the vast majority of stars were observed using the long, 30-minute cadence mode (Davenport 2016). Each continuous time segment was required to be at least two days in duration, and any segment less than two days in duration was discarded from analysis (Davenport 2016). Filter widths with lower limits of 6 hrs and upper limits of 24 hrs were used in the analysis of Yang and Liu (2019). If stellar flare durations are similar to solar flare durations, most of the stellar flares would not be resolved in low-cadence data from Kepler.

4.7. Background Subtraction Effect

The emitted radiation from flares in astrophysical objects contains almost always a flare-unrelated background flux in every wavelength, which could bias the measurement of the power law slope in a size distribution (Appendix A). This slope is severely modified in the lowest decade of a size histogram, while it does not affect the slope of large sizes. The background subtraction effect has been simulated in detail (Aschwanden 2015), which we corroborate with additional data given in Table 3. We sorted the power law measurements with subtracted background in the first column of Table 3, which yields a mean value of,

$$\alpha_E^{BG} = 1.57 \pm 0.19, \quad (34)$$

which is close to the theoretical prediction of the standard SOC model (i.e., $\alpha_E = 1.5$). There is also some statistics available from mostly GOES data without (or insufficient) background subtraction (Table 3, second column),

$$\alpha_E^{NBG} = 2.20 \pm 0.22, \quad (35)$$

which clearly corroborates the trend that the neglect of flare-unrelated background subtraction causes a mean bias of $(\alpha_E^{NBG} - \alpha_E^{BG}) \lesssim 0.6$ in the power law slope α_E . At this point we do not know how accurately the flare-unrelated background has been treated in the 75 stellar flare data sets discussed here (Tables 1 and 2). However, the fact that many power law slopes of the fluence size distribution exhibit values around $\alpha_E \approx 2$ (Fig. 5), lets us suspect that some of the high values could have been generated by inaccurate background subtractions.

While the empirical result of a power law slope of $\alpha_F \approx 2$ has been established for stellar flare events recently (Yang and Liu 2019), we are adding here a theoretical explanation for this finding that is predicted by SOC models. Taking the filtering of short flare durations in Kepler data into account, we find that the SOC model predicts the proportionalities $E_K \propto F$ (Eq. 32) and $F \propto V$ (Eq. 23), which implies the identities $\alpha_{EK} = \alpha_F = \alpha_V = 2$ and agrees with the observations generally (Fig. 5).

5. DISCUSSION

5.1. Flare Frequency and Stellar Rotation

The rotation period of a star is expected to be related to the star’s age, with younger stars rotating more rapidly, at least after their evolution of several 100 Myr on the main sequence; for younger stars, the rotation periods are widely distributed, depending on the “initial” rotation period (Johnstone et al. 2020). However it was found that the maximum energy of the flare is not correlated with the stellar rotation period, but the data suggest that superflares (with energies $E \geq 10^{33}$ erg) occur more frequently on rapidly rotating stars (Maehara et al. 2012). The frequency of superflares on slowly rotating stars was found to be smaller than that of all G-type dwarfs, and the frequency of superflares on hot G-type dwarfs ($5600 < T_{eff} < 6000$ K) is smaller than for cool G-type dwarfs ($5100 < T_{eff} < 5500$ K). In general, stars with shorter rotation periods tend to have larger power law slope values α . It has been confirmed that spots on flare stars are generally larger than those on non-flaring stars and that flare stars rotate significantly faster than non-flaring stars (Balona 2015). For stars in this sample with previously measured rotation periods, the total relative flare luminosity (Appendix B) has been compared to the Rossby number. A tentative detection of flare activity saturation for low-mass stars with rapid rotation below a Rossby number of ≈ 0.03 has been found (Davenport 2016). The rotation distribution of flare stars shows that about 70% of flare stars rotate with periods shorter than 10 days and the rate approaches 95% at 30 days (Yang and Liu 2019).

Comparing stellar flares from different spectral types involves often a strong detection bias. For instance, the bolometric luminosity of an M dwarf is very small compared to a G star, and thus smaller flares can be detected on M stars than on G stars for the same absolute sensitivity (Balona 2015). But it is also true that G stars can produce larger flares in absolute terms than M dwarfs (Johnstone et al. 2020).

5.2. *Nanoflares Versus Noise*

A lingering question in stellar observations is the unknown composite structure of apparently quiescent emission, especially from dM stars. In other words: Does quiescent emission entirely consist of Poisson noise, or is it made up of microflares (or nanoflares) that are part of a continuous size distribution extending with the same power law slope to large flares (Collura et al. 1988)? One would expect that this question can simply be settled by the characterization of their size distribution, which should be different for exponential-like or power law-like functions. Early observations of K and M dwarf stars with EXOSAT (Schmitt and Rosso 1988; Pallavicini et al. 1990; McGale et al. 1995) did not have sufficient sensitivity to detect coherent microflaring activity. The detection of the smallest flaring structures strongly depends on the detection threshold. Examination of EUV time profiles from RS CVn binaries reveals both, small-scale stochastic variability, as well as small flares (Osten and Brown 1999). More sensitive observations with Einstein-IPC did report continuous variability (Ambruster et al. 1987). Nearly continuous flaring in both X-rays and correlated fluxes in the U band were detected with EUVE (Audard et al. 2000; Guedel et al. 2002, 2004). In some samples of Kepler data, for instance, only flares have been included with total energies of $E \geq 5 \times 10^{34}$ erg (Shibayama et al. 2013). Those energies derived from Kepler observations are still orders of magnitudes more powerful than the largest solar flares $E \approx 10^{30} - 10^{33}$, while solar nanoflares have been detected down to $E \gtrsim 10^{24}$ erg (Krucker and Benz 1998; Parnell and Jupp 2000; Aschwanden and Parnell 2002).

The power law index of stellar size distributions ($\alpha_{EK} \approx 2.0$) is larger than for typical solar flares in hard X-rays ($\alpha_E \approx 1.5$), including small-scale solar events. If the power law continues to energies of moderate solar flares, then the total energy emitted by the ensemble of all flares may suffice to explain all of the observed flaring and “quiescent” X-ray emissions of flare stars. A considerable portion, if not all, of the energy required to heat their coronae could thus be provided by flares (Audard et al. 1999; 2000). The main result of this paper and of Yang and Liu (2019) is that stellar flares show a similar power law distribution slope of $\alpha \approx 2$ as solar flares do, and thus both solar and stellar flares (including microflares and nanoflares) are consistent with a common physical mechanism for flare heating and the coupled coronal heating.

5.3. *SOC in Stellar Flares*

What does it mean when we say that stellar flares exhibit self-organized criticality? If stellar flares would occur by pure random processes, their size distribution would fit a Poissonian or Gaussian function. In contrast, the fact that stellar flares are consistent with power law functions strongly supports the evolution of nonlinear (exponential-growing) energy dissipation processes, triggered by local fluctuations that exceed a system-wide threshold (Aschwanden 2011). The statistics of physical parameters in such nonlinear energy dissipation processes can be expressed with volumetric scaling laws, characterized by the scale-free probability (Eq. 19), the (spatial) fractal dimension (Eqs. 20, 21), classical diffusion (Eq. 22), the flux-volume scaling (Eq. 23), and the fluence scaling (Eqs. 24, 32). SOC models predict cross-correlations and power law size distributions with specific slopes in energy scaling laws, which can be tested with the observed parameters (Aschwanden 2020). The energy scaling laws depend strongly on the dimensionality and geometry of dissipation events. The spatio-temporal behavior of flare events may be governed by classical diffusion (Eq. 22). The fractal structure of a flaring region may quantify the self-similar geometry of the filling factor in a post-flare arcade. For stellar flares, we cannot test any spatial geometry due to the remoteness of the observed stars, so we cannot determine geometric slopes directly ($\alpha_L, \alpha_A, \alpha_V$), but we have four observed power law slopes that can be compared with predictions i.e., $\alpha_P = 5/3 = 1.67$ for the peak flux, $\alpha_F = 2$ for the mean flux, $\alpha_T = 2$ for the flare durations, and $\alpha_E = 3/2 = 1.5$ for the fluences. Since most of the quoted 20 publications provide the energy E only, we cannot fully test the SOC model with stellar flare data. Tests of the SOC model with solar flare data (Aschwanden et al. 2015, 2020), however, reveal encouraging results, although a number of improvements in the data analysis could be carried out (including data truncation, instrumental sensitivity threshold, preflare background subtraction, fine-size effects, etc.) (Aschwanden 2020), as demonstrated in Figs. 1-3.

6. CONCLUSIONS

We study the size distributions of stellar flare events, compiled from 20 publications, which contain a variety of 75 data sets from different stars and stellar spectral types, characterized by their power law slope α of their size distribution $N(x) \propto x^{-\alpha x}$. The largest data set comes from the Kepler mission, which produced a stellar flare catalog with 162,262 events, for which we perform high-precision modeling of its size distribution. We summarize the conclusions in order of the 5 initial questions.

1. What are the values and uncertainties of power law slopes in size distributions of stellar flares ? Size distributions of nonlinear events have generally been fitted with a power law function that extends over an arbitrary inertial range $[x_1, x_2]$, which causes large uncertainties in the slope value if the inertial range extends over a small range of 1-2 decades. This problem is ameliorated for the large stellar flare data set of the Kepler mission, which contains $n_{ev} \gtrsim 10^5$ events and covers an inertial range of $\lesssim 4$ decades in energy. A second source of uncertainties is the roll-over of the size distribution at small events (near x_1) due to incomplete sampling, data truncation, background subtraction, and instrumental sensitivity limitations, which can be adequately modeled with a thresholded power law or Pareto distribution. A third source of uncertainties is the neglect of an exponential drop-off at the upper end of the size distribution due to finite-system size effects, which can be modeled with an exponential function. A fourth uncertainty is the occasional presence of extreme events at the largest energies (near x_2) beyond the finite-system size effects, which are also called *Dragon-King events* and indicate a different (secondary) physical mechanism than the primary mechanism that produces the primary power law events. Taking all these effects into account, we find a best-fit power law slope value of $\alpha = 1.817 \pm 0.005$ for the entire Kepler data set. Averaging all 75 stellar data sets yields a range of $\alpha_{OPT} = 1.93 \pm 0.40$, while the largest 11 data sets with $n_{ev} > 1000$ events per set yield a range of $\alpha_{OPT} = 2.09 \pm 0.24$.
2. Do power law slopes vary with time ? We identified four M-dwarf stars with multiple observations of stellar flare size distributions during different times. We observe significant variations of the power law slope in time for YX CMi only, but they were measured with different instruments. Two other stars (AD Leo, CN Leo) show marginal variation. The variation in the power law slope $\alpha(t)$ could possibly indicate stellar magnetic cycles of order 5 – 20 years.
3. Do power law slopes of stellar flares depend on the spectral stellar type ? We find no significant deviations from the average power law slope $\alpha \approx 2$ for the spectral stellar types G, F, M, K, Giants. There is an outlier of $\alpha \approx 1.1$ for spectral type A in the study of Yang and Liu (2019), but automated fitting with our (P, F, E) models yield a more reliable value of $\alpha_E = 1.65$ for all 3 models (Aschwanden 2021), which implies that the outlier $\alpha = 1.1$ represents an erroneous value due to small-number statistics and an inadequately chosen fitting range.
4. Are stellar flare size distributions compatible with solar flares ? Comparing the fluence size distributions of solar flares observed with GOES in soft X-ray wavelengths ($\alpha_{F,GOES} = 1.98 \pm 0.11$) (Eq. 17) with those from Kepler observed in optical wavelengths ($\alpha_{F,OPT} = 2.09 \pm 0.24$) (Eq. 16), we find a good agreement between these two power law slopes, one measured in solar flares, the other in stellar flares. Furthermore, the Neupert effect observed in solar flares (Dennis and Zarro 1993) predicts a power law slope of $\alpha_{F,SXR} \propto \alpha_{E,HXR} = 2.0$. Strictly speaking, a proper comparison between solar and stellar flares would require white-light data from both instruments, which are sparsely available for solar data. The energy range of all Kepler flare events amounts to $E \approx 10^{34} - 4 \times 10^{38}$ erg, while solar flares cover a range of $E \approx 10^{24} - 10^{33}$ erg.
5. Are stellar flares consistent with self-organized criticality (SOC) models ? Standard SOC models predict power law slopes of $\alpha_F = 2.0$ for the mean flux, $\alpha_V = 2.0$ for the flare volume, and $\alpha_E = 1.5$ for the flare fluence, which changes to a value of $\alpha_{EK} = 2.0$ when the flare durations are not resolved or uncorrelated, which is the case in the analysis of low-cadence Kepler data cited here. Therefore we can conclude that white-light emissivity is proportional to the flare volume. Since the predicted values $\alpha_F = \alpha_V = \alpha_{EK} = 2.0$ overlap with the observed range of stellar flares, $\alpha_{OPT} = 2.09 \pm 0.24$, stellar size distributions are consistent with SOC models.

The Kepler mission has provided us an enormous wealth of stellar data, since stellar flares have been detected in a total of 3420 flare stars, while we had previously flare data from a single star (our Sun) only. Kepler detected a total of 162,262 stellar flares, which is a compatible with the largest solar flare data set, obtained from GOES (with 338,661 flare events). On the energetic side, the largest solar flare (with an energy of $E \lesssim 10^{33}$ erg) is still below the smallest flare detected with Kepler, with $E \gtrsim 10^{34}$ erg. Therefore, solar and stellar flare data sets are complementary in energy, but have very similar size distributions with power law slopes of $\alpha \approx 2$. Adding solar and stellar flares together would yield a combined size distribution that extends over 14 orders of magnitude (from 10^{24} erg to 10^{38} erg)! It needs to be shown that the same physical flare mechanism holds for such a large range of energies.

APPENDIX A: BACKGROUND SUBTRACTION IN SOLAR FLARES

One of the largest systematic uncertainties results from the preflare background subtraction, because the preflare flux is often not specified in solar flare catalogs. As long as the power law fits in size distributions of fluxes or fluences are applied in inertial ranges that are sufficiently above the background flux level, there is no problem with fitting power law slopes, but it introduces a systematic bias, typically from a slope of $\alpha_E \approx 1.5$ in background-subtracted data to $\alpha_E \approx 2.0$ for size distributions sampled without background subtraction. In the case of no background subtraction, the bias is always directed towards a steeper value, because the correction implies a relatively larger shift of small flares towards the right-hand side of a size distribution than for large flares. This effect has been simulated in detail in Fig. 3 of Aschwanden (2015).

On the observational side we find the following information on the preflare background in hard X-rays and gamma-rays: Early on, background subtraction was obtained manually between preflare background and peak flux (Drake 1971); HXRBS/SMM has a mean flare-unrelated background of ≈ 40 cts s^{-1} in the > 25 keV flux (Dennis et al. 1991; Crosby et al. 1993); ISEE-3 detects a mean background of ≈ 24 cts s^{-1} at > 50 keV, or 50 cts s^{-1} at > 30 keV (Bromund et al. 1995); background-subtracted data of gamma-ray flares are used from WATCH/GRANAT and GRS/SMM (Perez Enriquez and Mirochnishenko 1999); A global solar background with a 3-sigma threshold was set to detect microflares with RHESSI (Christe et al. 2008).

In soft X-ray wavelengths, reliable preflare background values can be obtained from images, such as from Yohkoh/SXT (Shimizu 1995). Flare detection using time profiles of GOES without background subtraction leads to a substantial bias for too steep power law slopes, which is the case in a number of studies: (Veronig et al. 2002a, 2002b; Yashiro et al. 2006). The preflare background has also been estimated from the absolute minimum of a time series encompassing each nanoflare (Krucker and Benz 2002; Benz and Krucker 2002), which yields a lower limit of the background fluence, and thus produces a similar bias as no background-subtraction. A similar search for nanoflares in TRACE data (Parnell and Jupp 2000) exhibits a sharp peak at the low end of the fluence size distribution, which is typical for under-estimated background subtraction (Aschwanden 2015). A more reliable background has been determined from imaging data, by mapping out the excess emission measure (associated with each nanoflare) in TRACE 171 and 195 filter data (Aschwanden et al. 2000b; Aschwanden and Parnell 2000a,b), or using SOHO/EIT imaging data (Uritsky et al. 2007, 2013).

In Table 3 we give a compilation of published solar flare size distributions of the fluence, $E = F T$, tabulated separately for studies that employed methods with preflare background subtraction (Table 3, first column), and without background subtraction (Table 3, second column). The systematic background subtraction bias can be clearly be seen when the two groups are averaged separately. While the background-subtracted samples yield a mean fluence value of $\alpha_E = 1.57 \pm 0.11$ (or a median value of 1.54), which agrees with the theoretically predicted value of $\alpha_E = 1.5$ according to the fractal-diffusive SOC model (Aschwanden 2015), while those statistics without preflare background subtraction yield a systematically higher value of $\alpha_E = 2.10 \pm 0.27$. Ideally, the preflare backgrounds should be subtracted for each flare event individually, but if this information is not available, at least a mean background value should be corrected.

APPENDIX B: THE KEPLER FLARE ENERGY DEFINITION

There are two measures to quantify the energy of a stellar flare: (i) the (background-subtracted) peak (flux) or amplitude of a stellar luminosity time profile $f_{flare}(t)$ in a given wavelength range $\lambda \pm \Delta\lambda$, which has a mean of $F_{flare} = \langle f_{flare}(t) \rangle$,

$$P_{flare} = \max[f_{flare}(t)] , \quad (B1)$$

and (ii) the time-integrated luminosity (intensity, or energy) E_{flare} ,

$$E_{flare} = \int f_{flare}(t) dt \approx F_{flare} T_{flare} , \quad (B2)$$

also called fluence or total energy, where T_{flare} is the flare duration.

For the energy measurements of the Kepler instrument, it is assumed that the spectrum of white-light flares can be described by a black-body radiation with an effective temperature of $T_{flare} = 10^4$ K and flare area $a_{flare}(t)$ (Shibayama et al. 2013),

$$f_{flare}(t) = \sigma_{SB} T_{flare}^4(t) a_{flare}(t) , \quad (B3)$$

with σ_{SB} the Stefan-Boltzmann constant. The flare area $a_{flare}(t)$ is estimated from the observed luminosity of the star (f'_{star}), the flare (f'_{flare}), and the flare amplitude of the light curve $f_{flare}(t)$ of Kepler after detrending,

$$f'_{star} = \int R_{\lambda} B_{\lambda(T_{eff})} d\lambda \cdot \pi R_{star}^2, \quad (B4)$$

$$f'_{flare}(t) = \int R_{\lambda} B_{\lambda(T_{flare}(t))} d\lambda \cdot a_{flare}(t), \quad (B5)$$

$$a_{flare}(t) = \pi R^2 \left(\frac{f'_{flare}}{f'_{star}} \right) \frac{\int R_{\lambda} B_{\lambda(T_{eff})} d\lambda}{\int R_{\lambda} B_{\lambda(T_{flare}(t))} d\lambda}, \quad (B6)$$

where $B_{\lambda(T)}$ is the Planck function, and R_{λ} is the response function of the Kepler instrument.

If we compare the total energy of a stellar flare observed by Kepler with solar flares, the corresponding quantity is the bolometric energy of white-light emission. However, white-light emission in solar flares is observed for the largest flares only, produced by $\gtrsim 5$ keV electrons and ions that precipitate into the deeper chromosphere and produce long-lived excess ionization in the heated chromosphere to enhance free-free and free-bound continuum emission, visible in broadened Balmer and Paschen lines (Hudson 1972). The ratio of bolometric energies E_{bol} to the thermal energy E_{th} of the flare plasma was found to be commensurable, i.e., $E_{bol}/E_{th} = 1.14 \pm 0.05$ (Kretzschmar 2011; Aschwanden et al. 2015, 2017).

Acknowledgements: Part of the work was supported by NASA contract NNG04EA00C of the SDO/AIA instrument and the NASA STEREO mission under NRL contract N00173-02-C-2035.

REFERENCES

- Ambruster, C.W., Sciortino, S., and Golub, L. 1987, *Rapid, low-level X-ray variability in active late-type dwarfs*, ApJS 65, 273
- Arzner, K. and Güdel, M. 2004, *Are coronae of magnetically active stars heated by flares? III. Analytical distribution of superposed flares*, ApJ 602, 363
- Arzner, K., Guedel, M., Briggs, K., Telleschi, A., and Audard, M. 2007, *Statistics of superimposed flares in the Taurus molecular cloud*, AA 468, 477
- Aschwanden, M.J., Nightingale, R., Tarbell, T., and Wolfson, C.J. 2000a, *Time variability of the quiet Sun observed with TRACE. I. Instrumental effects, event detection, and discrimination of EUV nanoflares*, ApJ 535, 1027
- Aschwanden, M.J., Tarbell, T., Nightingale, R., Schrijver, C.J., Title, A., Kankelborg, C.C., Martens, P.C.H., and Warren, H.P. 2000b, *Time variability of the quiet Sun observed with TRACE. II. Physical parameters, temperature evolution, and energetics of EUV nanoflares* ApJ 535, 1047
- Aschwanden, M.J. and Parnell, C.E. 2002, *Nanoflare statistics from first principles: fractal geometry and temperature synthesis*, ApJ 572, 1048
- Aschwanden, M.J. 2011, *Self-Organized Criticality in Astrophysics. The Statistics of Nonlinear Processes in the Universe*, ISBN 978-3-642-15000-5, Springer: New York
- Aschwanden, M.J., and Freeland, S.L. 2012, *Automated solar flare statistics in soft X-rays over 37 years of GOES observations: The invariance of self-organized criticality during three solar cycles*, ApJ 754:112
- Aschwanden, M.J. 2014, *A macroscopic description of a generalized self-organized criticality system: Astrophysical applications*, ApJ 782:54
- Aschwanden, M.J. 2015, *Thresholded powerlaw size distributions of instabilities in astrophysics*, ApJ 814, 19
- Aschwanden, M.J., Caspi, A., Cohen, C.M.S., Holman, G.D., Jing, J., Kretzschmar, M., Kontar E.P., McTiernan, J.M., et al. 2017, *Global energetics of solar flares: V. Energy closure*, ApJ 836:17
- Aschwanden, M.J. 2019, *Self-organized criticality in solar and stellar flares: Are extreme events scale-free ?* ApJ 880, 105
- Aschwanden, M.J. 2020, *Global energetics of solar flares. XII. Energy scaling laws*, ApJ 903:23
- Aschwanden, M.J. 2021, *Finite system-size effects in self-organized criticality systems*, ApJ, (subm.)
- Audard, M., Güdel, M., and Guinan, E.F. 1999, *Implications from extreme-ultraviolet observations for coronal heating of active stars*, ApJ 513, L53
- Audard, M., Guedel, M., Drake, J.J., and Kashyap, V.L. 2000, *EUV flare activity in late-type stars*, ApJ 541, 396
- Bak, P., Tang, C., and Wiesenfeld, K. 1987, *Self-organized criticality - An explanation of 1/f noise*, Physical Review Lett. 59/27, 381
- Bak, P., Tang, C., and Wiesenfeld, K. 1988, *Self-organized criticality*, Physical Rev. A 38/1, 364
- Benz, A.O. and S. Krucker 2002, *Energy distribution of micro-events in the quiet solar corona* ApJ 568, 413
- Borucki, W.J., Koch, D., Basri, G. et al. 2010, *Kepler planet-detection mission: Introduction and first results*, Science 327, 977
- Bromund, K.R., McTiernan, J.M., and Kane, S.R. 1995, *Statistical studies of ISEE3/ICE observations of impulsive hard X-ray solar flares* ApJ 455, 733
- Christe, S., Hannah, I.G., Krucker, S., McTiernan, J., and Lin, R.P. 2008, *RHESSI microflare statistics. I. Flare-finding and frequency distribution*, ApJ 677, 1385
- Clauset, A., Shalizi, C.R., and Newman, M.E.J. 2009, *Power-law distributions in empirical data* SIAM Review 51/4, 661
- Collura, A., Pasquini, L., and Schmitt, J.H.M.M. 1988, *Time variability in the X-ray emission of dM stars observed by EXOSAT*, AA 205, 197
- Crosby, N.B., Aschwanden, M.J., and Dennis, B.R. 1993, *Frequency distributions and correlations of solar flare X-ray flare parameters*, SoPh 143, 275.
- Davenport, J.R. 2016, *The Kepler Catalog of stellar flares*, ApJ 829:23
- Dennis, B.R., Orwig, L.E., Kennard G.S., Labow, G.J., Schwartz, R.A., Shaver, A.R., and Tolbert, A.K. 1991, *The complete Hard X-Ray Burst Spectrometer event list, 1980-1989* NASA Technical Memorandum 4332
- Dennis, B.R. and Zarro, D.M. 1993, *The Neupert effect: What can it tell us about the impulsive and gradual phases of solar flares*, SoPh 146, 177
- Drake, J.F. 1971, *Characteristics of soft solar X-ray bursts*, SoPh 16, 152

- Gizis, J.E., Paudel, R.R., Mullan, D.,Schidt, S.J., Burgasser, A.J., and Williamer, P.K.G. 2017, *K2 Ultracool dwarf survey. II. The white light flare rate of young brown dwarfs* ApJ 845:33
- Güdel, M., Audard, M., Skinner, S.L., and Horvath, M.I. 2002, *X-ray evidence for flare density variations and continual chromospheric evaporation in Proxima Centauri*, ApJ 580, L73
- Güdel, M., Audard, M., Kashyap, V.L., and Guinan, E.F. 2003, *Are coronae of magnetically active stars heated by flares? II. Extreme Ultraviolet and X-ray flare statistics and the differential emission measure distribution*, ApJ 582, 423
- Güdel, M., Audard, M., Reale, F., Skinner, S.L., and Linsky, J.L. et al. 2004, *Flares from small to large: X-ray spectroscopy of Proxima Centauri with XMM-Newton* AA 416, 713
- Hosking, J.M.R. and Wallis, J.R. 1987, *Parameter and quantile estimation for the generalized Pareto distribution*, Technometrics 29(3), 339.
- Hudson, H.S. 1972, *Thick target processes and white light flares*, SoPh 24, 414
- Johnstone, C.P., Bartel, M., and Güdel, M. 2020, *The active lives of stars: a complete description of rotation and XUV evolution of F, G, K, and M dwarfs?* AA (in press)
- Kashyap, V.L., Drake, J.J., Güdel, M., and Audard, M. 2002, *Flare heating in stellar coronae*, ApJ 580, 1118
- Kretzschmar, M. 2011, *The Sun as a star: observations of white-light flares*, AA 530, A84
- Krucker, S. and Benz, A.O. 1998, *Energy distribution of heating processes in the quiet solar corona*, ApJ 501, L213
- Lacy, C.H., Moffett, J.J., and Evans, D.S. 1976, *UV Ceti stars: statistical analysis of observational data*, ApJSS 30, 85
- Lomax, K.S. 1954, *Business Failures; Another example of the analysis of failure data*, J. Am. Stat. Assoc. 49, 847
- Maehara, H., Shibayama, T., Notsu, Y., Nagao, T., Kusaba, S., Honda, S., Nogami, D., and Shibata, K. 2012, *Superflares on solar-like stars*, Nature 485, 478
- McGale, P.A., Pye, J.P., Barber, C.R., and Page, C.G. 1995 *Temporal behaviour of sources in the ROSAT extreme-ultraviolet all-sky survey*, MNRAS 275, 1232
- Moffett, J.J. 1974, *UV Ceti flare stars observational data*, ApJSS 273, 29, 1
- Moffett, J.J. and Bopp, B.W. 1976, *UV Ceti stars: statistical analysis of observational data*, ApJSS 31, 61
- Osten, R.A. and Brown, A. 1999, *Extreme Ultraviolet Explorer (EUVE) photometry of RS Canum Venaticorum (RS CVn) systems: four flaring megaseconds*, ApJ 515, 746
- Pallavicini, R., Tagliaferri, G., and Stella, L. 1990, *X-ray emission from solar neighbourhood flare stars: a comprehensive survey of EXOSAT results*, AA 228, 403
- Parnell, C.E. and Jupp, P.E. 2000, *Statistical analysis of the energy distribution of nanoflares in the quiet Sun*, ApJ 529, 554
- Perez-Enriquez, R. and Miroshnichenko, L.I. 1999, *Frequency distributions of solar gamma ray events related and not related with SPEs in 1980-1995*, SoPh 188, 169
- Pruessner, G. 2012, *Self-organised criticality. Theory, models and characterisation*, ISBN 9780521853354, Cambridge University Press: Cambridge
- Robinson, R.D., Carpenter, K.G., and Percival, J.W. 1999, *A search for microflaring activity on dMe flare stars. II. Observations of YZ Canis Minoris*, ApJ 516, 916
- Schmitt J.H.M.M. and Rosso, C. 1988, *EXOSAT observations of M dwarf stars in the solar neighborhood*, AA 191, 99
- Shibayama, T., Maehara, H., Notsu, S., Nosu, Y., Nagao, T., Honda, S., Ishi, T.T., Nogami, D., and Shibata, K. 2013, *Superflares on solar-type stars observed with Kepler. I. Statistical properties of superflares*, ApJSS 209:5
- Shimizu, T. 1995, *Energetics and occurrence rate of active-region transient brightenings and implications for the heating of the active-region corona*, PASJ 47, 251
- Sornette, D. 2009, *Dragon-King, black swans and the prediction of crises*, J. Terraspace Science and Engineering, 2, 1
- Sornette, D. and Ouillon, G. 2012, *Dragon-Kings: Mechanisms, statistical methods and empirical evidence*, EPJST 205, 1
- Stelzer, B., Flaccomio, E., Briggs, K., Micela, G., Scelsi, L, Audard, M., Pillitteri, I., and Güdel, M. 2007, *A statistical analysis of X-ray variability in pre-main sequence objects of the Taurus molecular cloud*, AA 468, 463
- Uritsky, V.M., Paczuski, M., Davila, J.M., and Jones, S.I. 2007, *Coexistence of Self-Organized Criticality and Intermittent Turbulence in the Solar Corona*, Phys.Rev.Lett. 99, 025001
- Uritsky, V.M., Davila, J.M., Ofman, L., and Coyner, A.J. 2013, *Stochastic Coupling of Solar Photosphere and Corona*, ApJ 769, 62

- Van Doorselaere, T., Hoda, S., and Deboscher J. 2017, *Stellar flares observed in long-cadence data from the Kepler mission*, *ApJSS* **232:26**.**
- Veronig, A.M., Temmer, M., Hanslmeier, A., Otruba, W., and Messerotti, M. 2002a, *Temporal aspects and frequency distributions of solar soft X-ray flares*, *AA* 382, 1070
- Veronig, A.M., Temmer, M., and Hanslmeier, A. 2002b, *Frequency distributions of solar flares*, *Hvar Observatory Bulletin*, 26, 7
- Wu, C.J., Ip, W.H., and Huang, L.C. 2015, *A study of variability in the frequency distributions of the superflares of G-type stars observed by the Kepler mission*, *ApJ* 798:92
- Yang, H. and Liu, J. 2019, *The flare catalog and the flare activity in the Kepler mission*, *ApJSS* 241:1
- Yashiro, S., Akiyama, S., Gopalswamy, N., and Howard, R.A. 2006, *Different Power-Law Indices in the Frequency Distributions of Flares with and without Coronal Mass Ejections*, *ApJ* 650, L143

Table 1. The power law slopes of the frequency distributions of energies observed in stellar flares: α for the differential frequency distribution, and $\alpha = \beta + 1$ for the cumulative size distributions.

| Star | Spectral type | Instrument | Number of flares or events | Differential slope α | Cumulative slope plus 1 $\beta + 1$ | Reference |
|-------------------|---------------|------------|----------------------------|-----------------------------|-------------------------------------|-------------------------|
| CN Leo | dM6.5 Ve | UBV | 111 | 1.99±0.19 | 1.99 ± 0.12 | Lacy et al. 1976 |
| UV Cet | M6.0e | UBV | 107 | 1.98±0.19 | 1.98 ± 0.14 | Lacy et al. 1976 |
| Wolf 424 AB | M5.5 | UBV | 11 | 1.81±0.54 | 1.81 ± 0.18 | Lacy et al. 1976 |
| YZ CMi | M5 V | UBV | 62 | 1.71±0.22 | 1.71 ± 0.08 | Lacy et al. 1976 |
| EQ Peg | M4 Ve | UBV | 58 | 2.00±0.26 | 2.00 ± 0.14 | Lacy et al. 1976 |
| EV Lac | M3.5 | UBV | 22 | 1.69±0.36 | 1.69 ± 0.11 | Lacy et al. 1976 |
| AD Leo | M3.5eV | UBV | 9 | 1.82±0.61 | 1.82 ± 0.27 | Lacy et al. 1976 |
| YY Gem | dM1e | UBV | 6 | 1.43±0.58 | 1.43 ± 0.11 | Lacy et al. 1976 |
| M dwarfs | dM | EXOSAT | 13 | 1.52±0.42 | | Collura et al. 1988*) |
| M dwarfs | dM | EXOSAT | 20 | 1.70±0.10 | | Pallavicini et al. 1990 |
| RS CVns | G | EUVE | 30 | 1.60±0.32 | | Osten and Brown 1999 |
| YZ CMi | M5 V | HSP/HST | 54 | 2.25±0.31 | 2.25 ± 0.10 | Robinson et al. 1999 |
| G dwarfs | G | EUVE | 25 | 2.15±0.15 | | Audard et al. 1999 |
| HD 2726 | F2 V | EUVE | 15 | 2.43±1.07 | 2.61±0.38 | Audard et al. 2000 |
| 47 Cas | G0-5 V | EUVE | 12 | 2.62±1.85 | 2.19±0.34 | Audard et al. 2000 |
| EK Dra | G1.5 V | EUVE | 15 | 1.78±0.62 | 2.08±0.34 | Audard et al. 2000 |
| κ Cet 1994 | G5 V | EUVE | 5 | 2.55±0.31 | 2.18±0.89 | Audard et al. 2000 |
| κ Cet 1995 | G5 V | EUVE | 10 | 2.45±1.08 | 2.29±0.51 | Audard et al. 2000 |
| AB Dor | K1 V | EUVE | 16 | 1.76±0.74 | 1.88±0.26 | Audard et al. 2000 |
| ϵ Eri | K2 V | EUVE | 12 | 2.38±1.50 | 2.40±0.81 | Audard et al. 2000 |
| GJ 411 | M2 V | EUVE | 15 | 1.57±0.57 | 1.63±0.29 | Audard et al. 2000 |
| AD Leo | M3.5 V | EUVE | 12 | 1.65±1.17 | 2.02±0.28 | Audard et al. 2000 |
| EV Lac | M4.5 V | EUVE | 12 | 1.75±1.18 | 1.76±0.33 | Audard et al. 2000 |
| CN Leo 1994 | M6.5 Ve | EUVE | 13 | 2.24±0.63 | 2.21±0.30 | Audard et al. 2000 |
| CN Leo 1995 | M6.5 Ve | EUVE | 15 | 1.59±0.86 | 1.46±0.39 | Audard et al. 2000 |
| FK Aqr | dM2e | EUVE | 65 | 2.60±0.34 | | Kashyap et al. 2002 |
| V1054 Oph | M3 Ve | EUVE | 85 | 2.74±0.35 | | Kashyap et al. 2002 |
| AD Leo | M3.5 V | EUVE | 80 | 2.17±0.03 | | Kashyap et al. 2002 |
| AD Leo | M3.5 V | EUVE | 75 | 2.32±0.11 | | Kashyap et al. 2002 |
| AD Leo | M3.5 V | EUVE | ? | 2.25±0.25 | | Güdel et al. 2003 |
| AD Leo | M3.5 V | EUVE | ? | 2.30±0.10 | | Arzner& Güdel 2004 |
| HD 31305 | M, K | XMM-Newton | ? | 2.20±0.30 | | Arzner et al. 2007 |
| TMC | M, K | XMM-Newton | ? | 2.40±0.50 | | Stelzer et al. 2007 |

*) The flare fluxes from multiple stars were co-added without distance correction in Collura et al. (1988).

Table 2. The power law slopes of the frequency distributions of energies observed in stellar flares with Kepler: α for the differential frequency distribution, and $\alpha = \beta + 1$ for the cumulative size distributions.

| Star | Instrument | Number of flares and events | Differential slope α | Cumulative slope plus 1 $\beta + 1$ | Reference |
|-------------------|------------|-----------------------------------|-----------------------------------|---|----------------------------------|
| G5-stars | Kepler | 365 | 2.30±0.30 | | Maehara et al. 2012 |
| G5-stars slow | Kepler | 101 | 2.00±0.20 | | Maehara et al. 2012 |
| G5-stars | Kepler | 1547 | 2.20±0.06 | | Shibayama et al. 2013 |
| G5-stars slow | Kepler | 397 | 2.00±0.10 | | Shibayama et al. 2013 |
| G5-stars | Kepler | 1538 | 2.43±0.08 | 2.42±0.06 | Aschwanden 2015 |
| G-type stars | Kepler | 4494 | 2.04±0.17 | | Wu et al. 2015 |
| K-M,A-F stars | Kepler | 209 | 1.69±0.16 | 1.71±0.12 | Balona 2015, Aschwanden 2015 |
| KID3557532 | Kepler | 196 | 2.11±0.19 | | Wu et al. (2015) |
| KID6034120 | Kepler | 45 | 3.12±0.60 | 3.17±0.48 | Aschwanden 2015 |
| KID6697041 | Kepler | 37 | 1.83±0.37 | 1.51±0.25 | Aschwanden 2015 |
| KID6865416 | Kepler | 147 | 1.77±0.10 | | Wu et al. 2015 |
| KID75264976 | Kepler | 40 | 1.92±0.34 | 1.98±0.32 | Aschwanden 2015 |
| KID7532880 | Kepler | 159 | 1.90±0.16 | | Wu et al. 2015 |
| KID8074287 | Kepler | 160 | 1.87±0.10 | | Wu et al. 2015 |
| KID8479655 | Kepler | 39 | 1.45±0.23 | 1.47±0.24 | Aschwanden 2015 |
| KID8547383 | Kepler | 40 | 3.41±0.68 | 2.58±0.41 | Aschwanden 2015 |
| KID9653110 | Kepler | 158 | 1.64±0.07 | | Wu et al. 2015 |
| KID10422252 | Kepler | 177 | 1.75±0.08 | | Wu et al. 2015 |
| KID10422252 | Kepler | 57 | 2.99±0.58 | 2.78±0.37 | Aschwanden 2015 |
| KID10745663 | Kepler | 137 | 1.63±0.10 | | Wu et al. 2015 |
| KID11551430 | Kepler | 202 | 1.59±0.06 | | Wu et al. 2015 |
| Stellar flares | Kepler | 208 | 1.68±0.12 | | Aschwanden 2019 |
| Bolometric flares | Kepler | 1537 | 2.55±0.07 | | Aschwanden 2019 |
| KID10000490 | Kepler | 241 | | 1.55±0.10 | Davenport 2016 |
| KID10001145 | Kepler | 271 | | 2.40±0.15 | Davenport 2016 |
| KID10001154 | Kepler | 119 | | 1.56±0.14 | Davenport 2016 |
| KID10001167 | Kepler | 147 | | 1.41±0.12 | Davenport 2016 |
| KID10007792 | Kepler | 225 | | 1.52±0.10 | Davenport 2016 |
| KID10002897 | Kepler | 155 | | 1.28±0.10 | Davenport 2016 |
| KID10004510 | Kepler | 142 | | 1.43±0.12 | Davenport 2016 |
| KID10004660 | Kepler | 135 | | 1.83±0.24 | Davenport 2016 |
| KID10005966 | Kepler | 175 | | 1.79±0.14 | Davenport 2016 |
| KID10006158 | Kepler | 279 | | 1.85±0.11 | Davenport 2016 |
| A-type | Kepler | 583 | 1.12±0.08 | 1.65 ± 0.07 | Yang & Liu 2019, Aschwanden 2021 |
| F-type | Kepler | 8869 | 2.11±0.09 | 1.85 ± 0.09 | Yang & Liu 2019, Aschwanden 2021 |
| G-type | Kepler | 55259 | 1.96±0.04 | 1.79 ± 0.06 | Yang & Liu 2019, Aschwanden 2021 |
| K-type | Kepler | 47112 | 1.78±0.02 | 1.80 ± 0.20 | Yang & Liu 2019, Aschwanden 2021 |
| M-type | Kepler | 50439 | 2.13±0.05 | 1.84 ± 0.02 | Yang & Liu 2019, Aschwanden 2021 |
| Giants | Kepler | 6496 | 1.90±0.10 | 2.00 ± 0.34 | Yang & Liu 2019, Aschwanden 2021 |
| All | Kepler | 162262 | | 1.823±0.007 | This work |

Table 3. The power law slopes of the frequency distributions of solar flare fluences α_E , calculated with preflare background subtraction (first column) or without any background subtraction (second column).

| Powerlaw slope of fluence α_E background subtracted | Powerlaw slope of fluence α_E no background subtracted | Number of events n_{ev} | Wavelength or energy threshold | Instrument | Reference |
|--|---|---------------------------------|-----------------------------------|-----------------|-------------------------------|
| 1.53±0.02 | | 7045 | >25 keV | HXRBS/SMM | Crosby et al. 1993 |
| 1.71±0.04 | | 1008 | >25 keV | HXRBS/SMM | Crosby et al. 1993 |
| 1.68±0.07 | | 545 | >25 keV | HXRBS/SMM | Crosby et al. 1993 |
| 1.67±0.03 | | 3874 | >25 keV | HXRBS/SMM | Crosby et al. 1993 |
| 1.69±0.02 | | 4356 | >30 keV | ISEE-3 | Bromund et al. 1995 |
| 1.80±0.01 | | 110 | >100 keV | PHEBUS, GRS/SMM | Perez Enriquez et al. (1999) |
| 1.38±0.01 | | 110 | >75 keV | PHEBUS, GRS/SMM | Perez Enriquez et al. (1999) |
| 1.39±0.01 | | 185 | >300 keV | PHEBUS, GRS/SMM | Perez Enriquez et al. (1999) |
| 1.30±0.01 | | 67 | >300 keV | PHEBUS, GRS/SMM | Perez Enriquez et al. (1999) |
| 1.50±0.03 | | 67 | >511 keV | PHEBUS, GRS/SMM | Perez Enriquez et al. (1999) |
| 1.39±0.02 | | 67 | >2223 keV | PHEBUS, GRS/SMM | Perez Enriquez et al. (1999) |
| 1.31±0.02 | | 67 | >1000 keV | PHEBUS, GRS/SMM | Perez Enriquez et al. (1999) |
| 1.39±0.01 | | 134 | >1000 keV | PHEBUS, GRS/SMM | Perez Enriquez et al. (1999) |
| 1.70±0.10 | | 4241 | >12 keV | RHESSI | Christe et al. (2008) |
| 1.44 | | 4028 | 2-12 Å | Explorer | Drake (1971) |
| 1.55±0.05 | | 5008 | 1265 Å | Yohkoh/SXT | Shimizu (1995) |
| | 2.03±0.09 | | 0.5-4 Å | GOES | Veronig et al. (2002a) |
| | 1.89±0.10 | | 0.5-4 Å | GOES | Veronig et al. (2002b) |
| | 2.01±0.03 | | 0.5-4 Å | GOES | Yashiro et al. 2006 |
| | 2.3-2.6 | | 171, 195 Å | SOHO/EIT | Krucker and Benz (1998) |
| | 2.0-2.6 | | 171, 195 Å | TRACE,SOHO/EIT | Parnell and Jupp (2000) |
| 1.79±0.08 | | | 171, 195 Å | TRACE | Aschwanden et al. (2002a,b) |
| | 2.31-2.59 | | 171, 195 Å | SOHO/EIT | Benz and Krucker (2002) |
| | 2.04-2.52 | | 171, 195 Å | SOHO/EIT | Benz and Krucker (2002) |
| 2.06±2.10 | | | 171 Å | TRACE | Aschwanden and Parnell (2002) |
| 1.70±0.17 | | | 195 Å | TRACE | Aschwanden and Parnell (2002) |
| 1.41±0.09 | | | AlMg | Yohkoh/SXT | Aschwanden and Parnell (2002) |
| 1.54±0.03 | | | 171, 195, AlMg | Yohkoh/SXT | Aschwanden and Parnell (2002) |
| 1.66-1.70 | | | EUV | SOHO/EIT | Uritsky et al. (2007) |
| 1.54±0.03 | | | 171, 195 | SOHO/EIT | Uritsky et al. (2013) |
| 1.57±0.19 | 2.20±0.22 | | | | Mean observed value |
| 1.54 | 2.28 | | | | Median observed value |
| 1.50 | | | | | SOC model prediction |

Kepler Stellar Flare Catalog (P-Model: Pareto distribution)

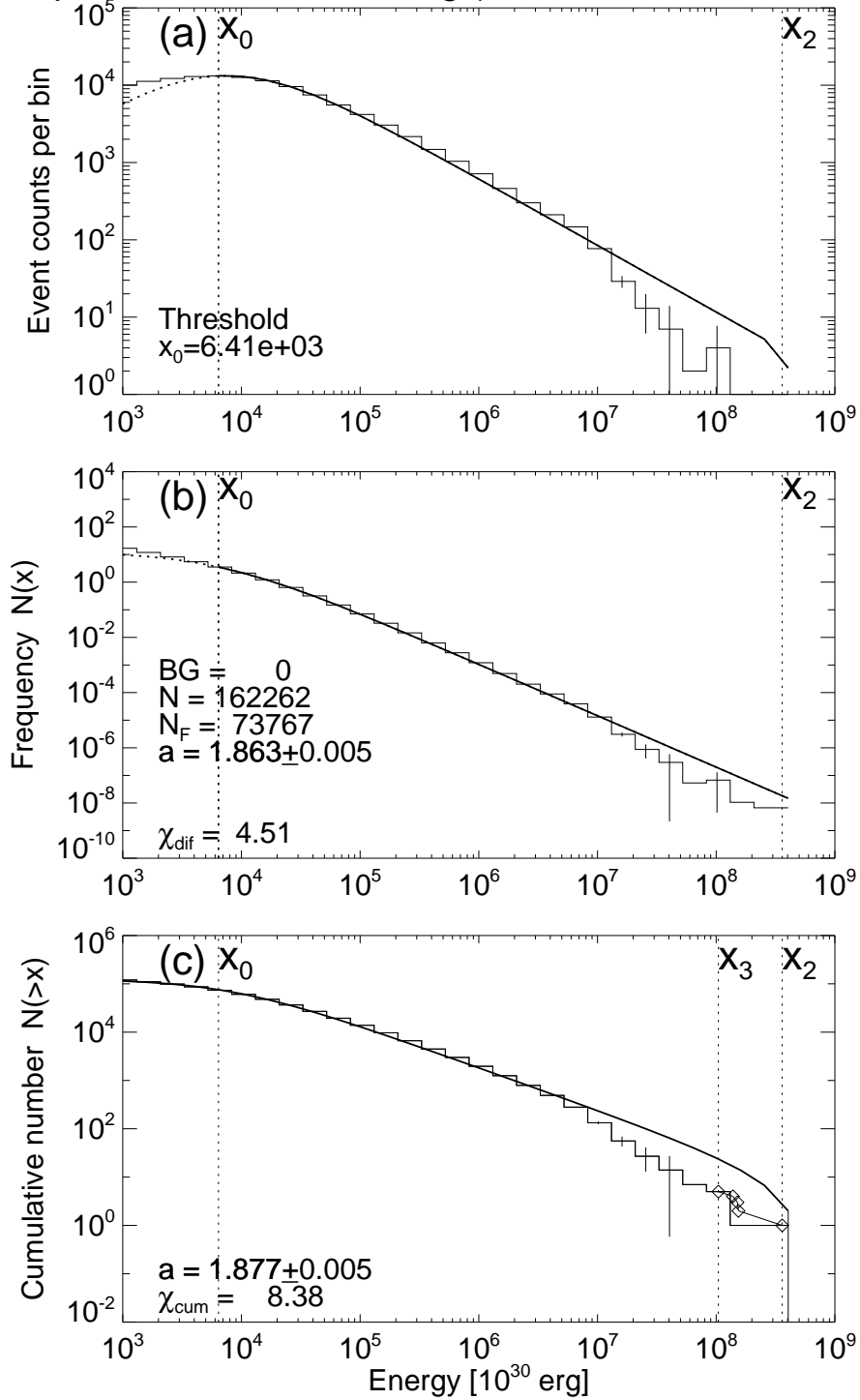


Figure 1. (a) Flare event counts in (logarithmic) histogram bins; (b) differential occurrence frequency distribution; (c) cumulative occurrence frequency distribution; and the rank-order bins of the 5 largest events (diamonds). The entire Kepler stellar flare catalog contains 162,262 events. A thresholded power law (Pareto distribution) function is shown (with solid curves), which represents an approximate model of the undersampling of small events.

Kepler Stellar Flare Catalog (F-Model: Finite system size)

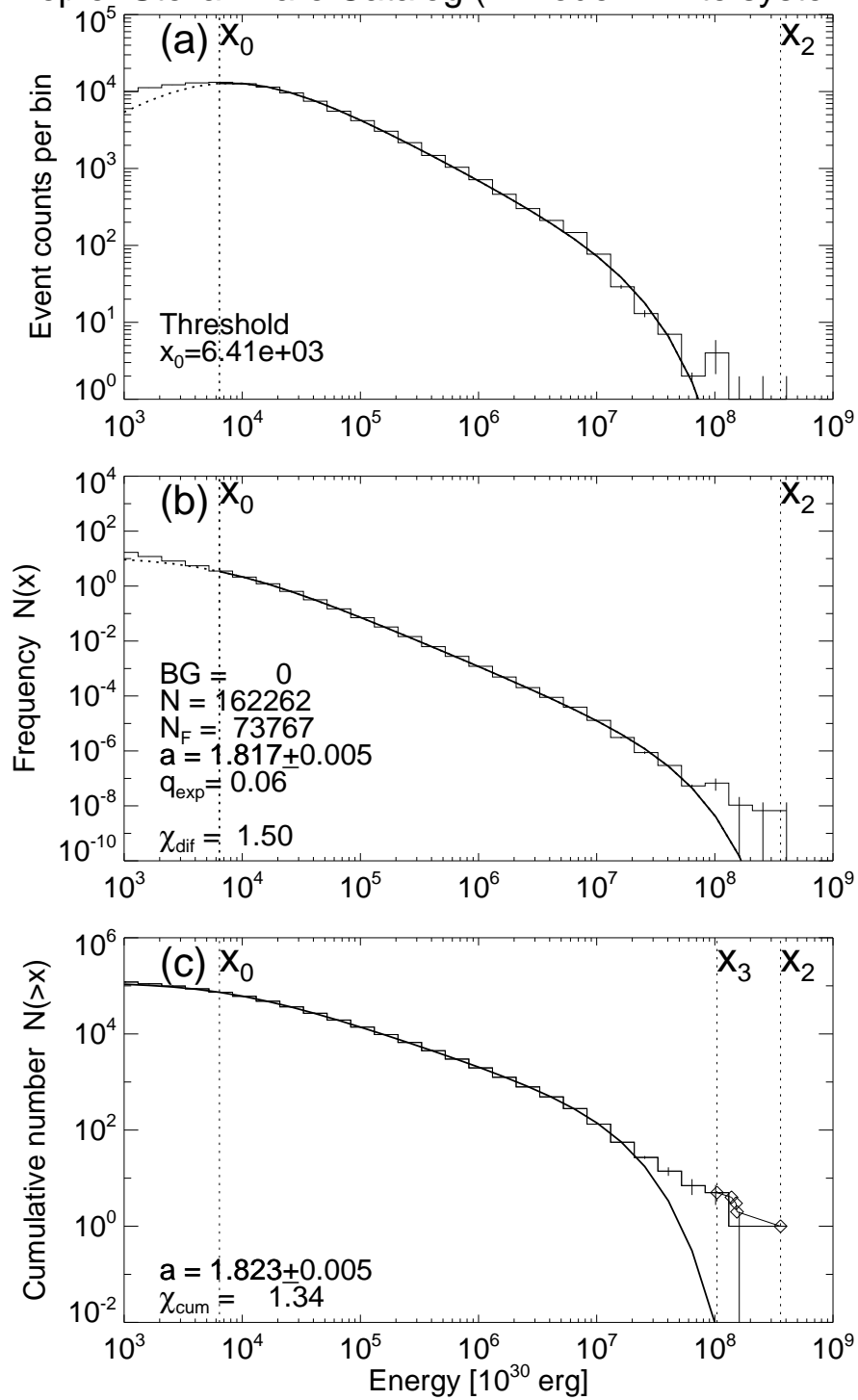


Figure 2. Stellar flare events from Kepler data base are fitted with an exponential drop-off function that models finite system size effects. Otherwise similar representation as in Fig. 1.

Kepler Stellar Flare Catalog (E-Model: Extreme events)

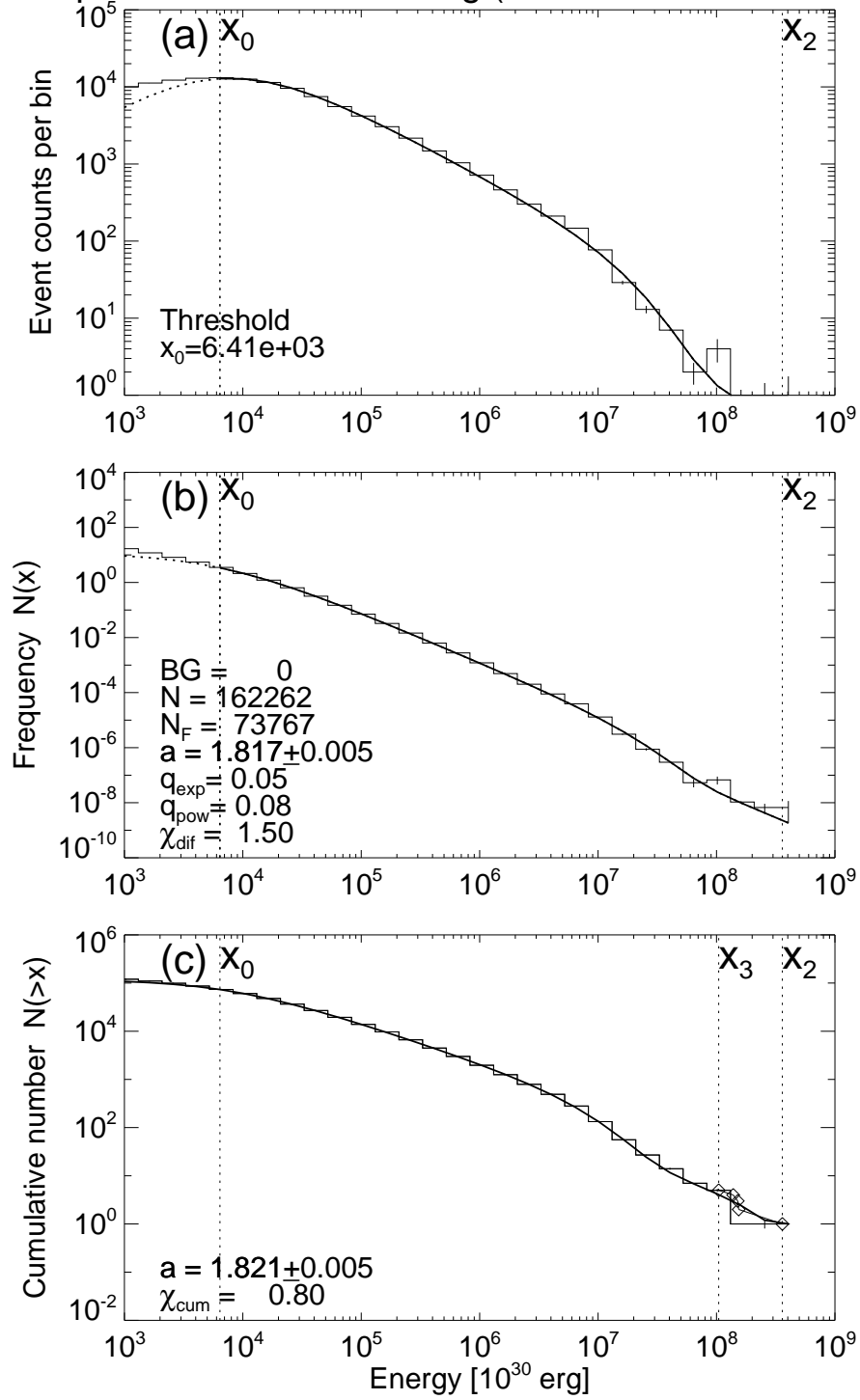


Figure 3. Stellar flare extreme events from Kepler data base are fitted with a secondary power law component. Otherwise similar representation as in Figs. 1 and 2.

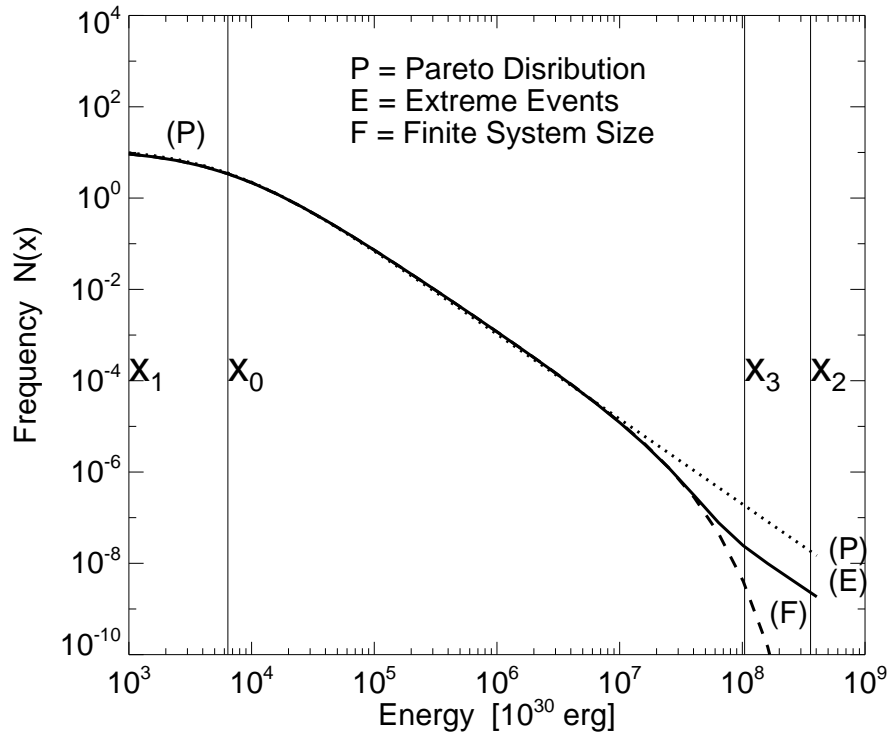


Figure 4. Synopsis of three power law models: (P) = Pareto distribution $[x_1, x_0]$, (E) = Extreme events $[x_3, x_2]$, and (F) = Finite system size model $[\lesssim x_3]$. The inertial range covers $[\gtrsim x_0, \lesssim x_3]$.

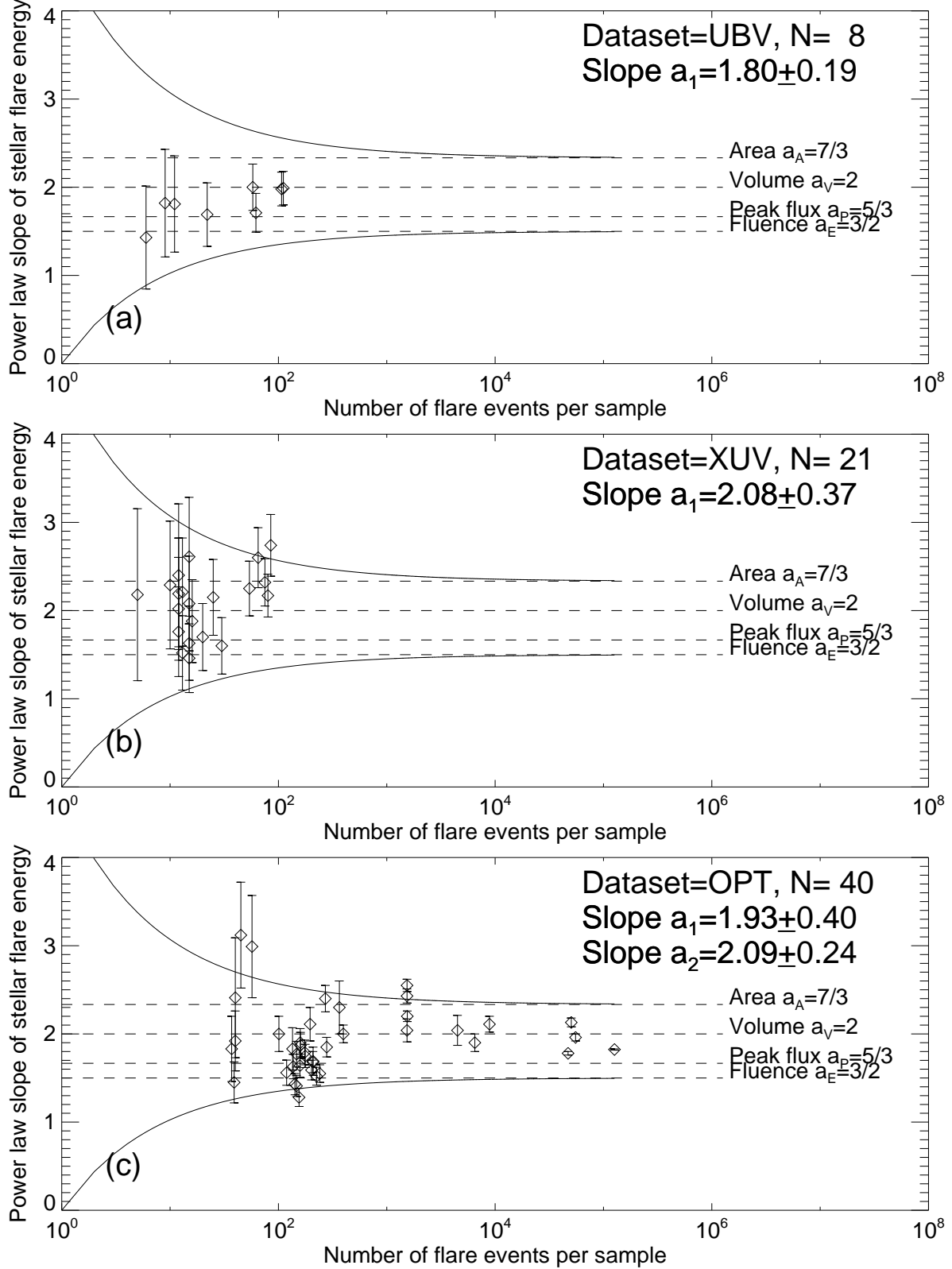


Figure 5. The power law slopes (α) of flare energy distributions as a function of the number of events per sample are shown separately for three instrument groups or wavelength ranges: UBV (a), XUV [EXOSAT, EUV, HSP/HST, XMM-Newton] (b), and OPT [Kepler] (c). The solid curves bracket the range of statistical uncertainties. The dashed horizontal lines indicate the predicted slopes of four SOC parameters: for the size distribution of the flare volume ($\alpha_V = 2$), the flare area ($\alpha_A = 7/3 = 2.33$), the peak flux ($\alpha_P = 5/3$), and the time-integrated flare energy or fluence ($\alpha_E = 3/2 = 1.5$). The slope a_1 includes all data sets, the slope a_2 samples with large statistics only ($n_{ev} \geq 1000$).

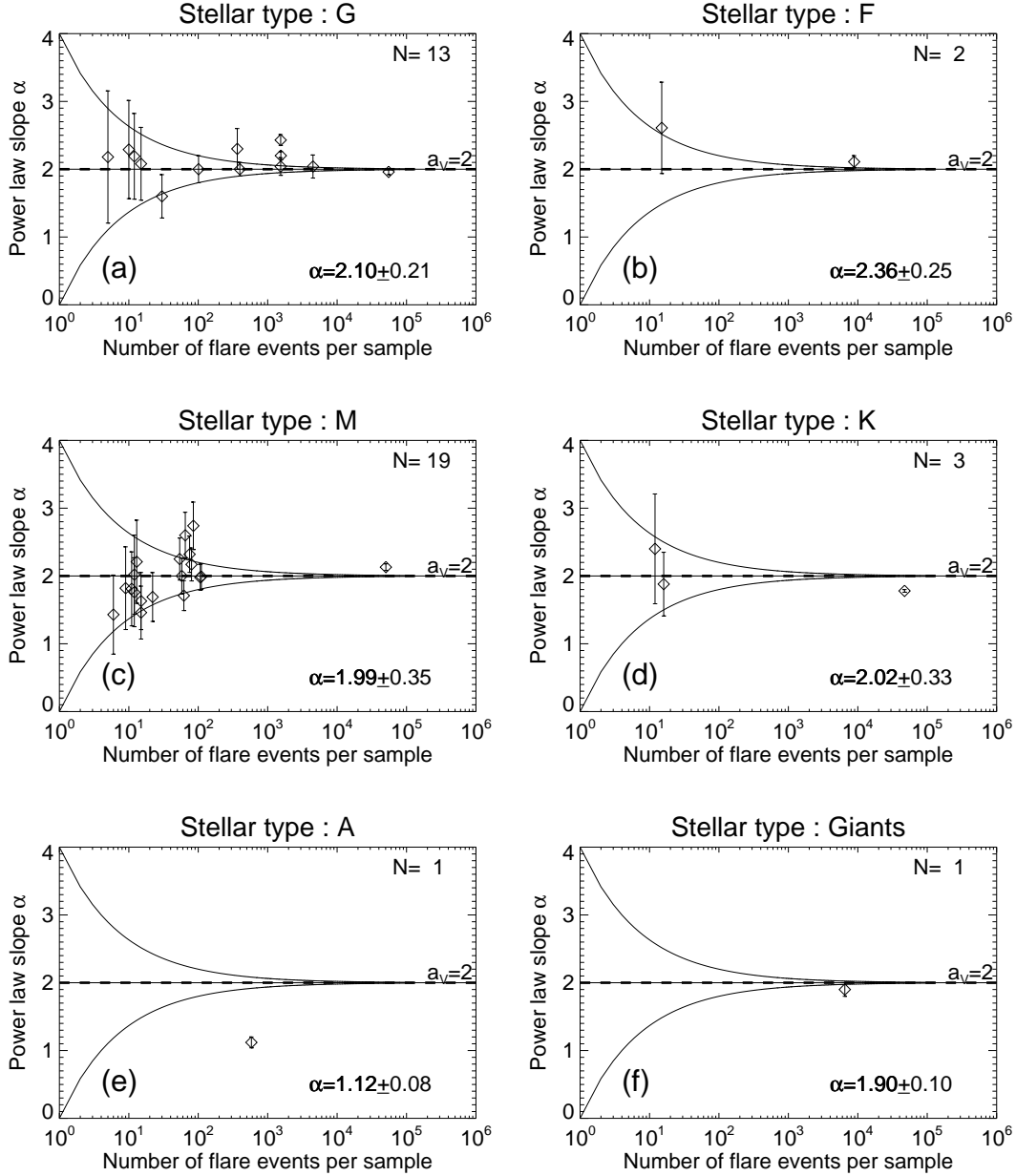


Figure 6. Means and standard deviations of power law slopes from data sets grouped by star types (A, F, G, K, M, Giants), based on the classification of the Kepler flare catalog (Yang and Liu 2019) and the star classification given in Tables 1 and 2.. The dashed horizontal lines indicate power law slopes predicted by a SOC model with $\alpha_V = 2$, while the curves indicate the expected uncertainties according to Eq. 12. The number of flare data sets per stellar spectral type varies from $N = 1$ (A-type stars) to $N = 13$ (G-type stars).

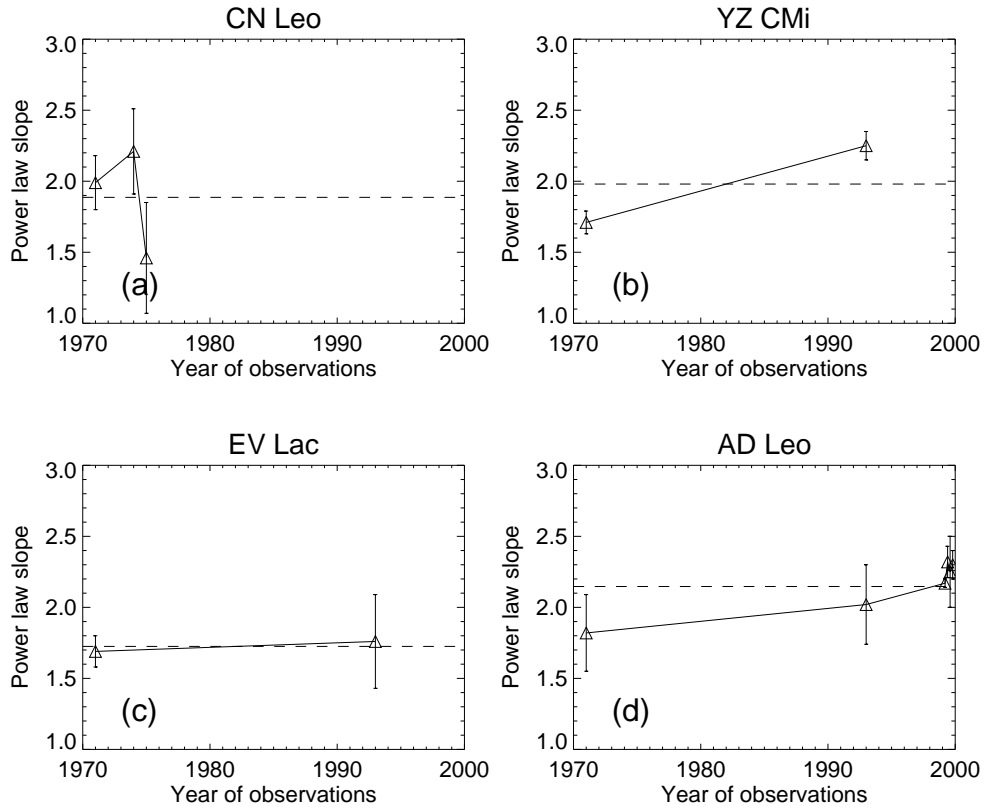


Figure 7. Time evolution of the power law slope $\alpha(t)$ of stellar flare energies observed in four stars (CN Leo, YZ CMi, EV Lac, and AD Leo). The error bars are computed from the standard deviation $\sigma_\alpha = \alpha/\sqrt{n}$, and the average value is indicated with a dashed horizontal line.